ISTITUTO NAZIONALE DI FISICA NUCLEARE
Laboratori Nazionali di Frascati

FRASCATI PHYSICS SERIES

Fifth Young Researchers Workshop "Physics Challenges in the LHC Era" 2016

Editor: Enrico Nardi

FRASCATI PHYSICS SERIES

Series Editor

Rossana Centioni

Technical Editor

Debora Bifaretti

Cover by Claudio Federici

Volume LXIII

Istituto Nazionale di Fisica Nucleare – Laboratori Nazionali di Frascati
Divisione Ricerca
SIDS – Servizio Informazione e Documentazione Scientifica
Ufficio Biblioteca e Pubblicazioni
P.O. Box 13, I-00044 Frascati Roma Italy
email: sis.publications@lnf.infn.it

Copyright © 2016 by INFN

All rights reserved. No part of this publication may be reproduced, stored in a retrieval system or transmitted in any form or by any means, electronic, mechanical, photocopying, recording or otherwise, without the prior permission of the copyright owner.

ISBN 978-88-86409-82-7

Fifth Young Researchers Workshop
“Physics Challenges in the LHC Era”
2016

International Scientific Committee:

Wilfried Buchmuller (DESY)
Filippo Ceradini (U. & INFN Roma3)
Anna DiCiaccio (U. & INFN Tor Vergata)
John Ellis (CERN & King's College, London)
Benjamin Grinstein (UC San Diego)
Ida Peruzzi (INFN-LNF & U. Perugia)
Antonio Pich (U. Valencia & IFIC, U. Valencia)

Local Organizing Committee:

Mario Antonelli
Mohamed Sofiane Boucenna
Gennaro Corcella
Vittorio Del Duca
Claudio Gatti
Martin Krauss
Davide Meloni
Andrea Longhin
Enrico Nardi (School Director)
Tommaso Spadaro

CONTENTS

PREFACE

The fifth Young Researcher Workshop "Physics Challenges in the LHC Era" was held in the Frascati National Laboratories during May 9^{th} and 13^{th} 2016, in conjunction with the XVIII edition of the Frascati Spring School "Bruno Touschek".

The Frascati Young Researcher Workshops started with the 2009 Frascati Spring School, and by now represent a well established and important appointment for graduate students in theoretical and experimental high energy and astroparticle physics. Young researchers are invited to present the results of their research work in a fifteen minutes talk, and discuss them with their colleagues. Students have to learn how to condense their results in a short presentation, how to organize a speech on a specialized subject in a way understandable to their colleagues, they get a training in preparing the write up of their contribution for the Workshop Proceedings, they experience how to interact with the Scientific Editor and with the Editorial Office of the Frascati Physics Series and, in many cases, their learn for the first time the procedure to submit their contribution in the arXiv.org database. Helping to develop all these skills is an integral part of the scientific formation the Frascati Spring School is providing.

These proceedings collect the joint efforts of the speakers of the Young Researchers Workshop 2016. The short write-ups represent the best demonstration of the remarkable scientific level of the Workshop contributors, and set the benchmark for the scientific level required to apply for participating in the Workshop.

The success of the XVIII Frascati Spring School "Bruno Touschek" and of the joint 5th Young Researcher Workshop "Physics Challenges in the LHC Era" relies on the efforts of a close-knit and well geared team of colleagues. A special acknowledgment goes to Maddalena Legramante, that carried out with her usual efficiency the secretariat work both for the Workshop and for the Spring School, to Claudio Federici, that always puts a special dedication in realizing the beautiful graphics for the Spring School posters and front page of the proceedings, and to Debora Bifaretti for the technical editing. I also want to thank the director of the LNF Research Division Paola Gianotti, the responsabile of the SIDS Rossana Centioni, and the responsabile of the LNF seminars Patrizia de Simone, for sponsoring the XVIII Spring School and for their precious help. Finally, a special thanks goes to the Director of the Frascati Laboratories, Dr. Pierluigi Campana, for his encouragement and unconditional support.

Frascati, 12 October 2016 *Enrico Nardi*

DISCRETE DARK MATTER MODEL AND REACTOR MIXING ANGLE

J. M. Lamprea*
Institute of Physics, UNAM, A.P. 20-364, Mexico City 01000, Mexico

Abstract

We present a scenario where the stability of dark matter and the phenomenology of neutrinos are related by the breaking of a flavour symmetry. We propose two models based on this idea for which we have obtained interesting neutrino and dark matter phenomenology.

1 Introduction

We propose an extension of the SM in the context of the discrete dark matter (DDM) mechanism [1]. This mechanism is based upon the fact that the breaking of a discrete non-Abelian flavour symmetry accounts for the neutrino masses and mixing pattern and for the dark matter stability. In the original DDM model A_4 is considered as the flavour symmetry and the particle content includes four $SU(2)$ Higgs doublets, the triplet $\eta = (\eta_1, \eta_2, \eta_3)$, and the SM

Higgs H as a singlet, four right-handed neutrinos, three of them in a triplet representation, $N_T = (N_1, N_2, N_3)$, and N_4 as a singlet. The lepton doublets L_i and the right charged ones l_i transform as the three different singlets of A_4 such that, the mass matrix for the charged leptons is diagonal. Breaking the A_4 symmetry into a Z_2, through the electroweak symmetry breaking, provides the stability mechanism for the DM and accounts for the neutrino masses and mixing patterns by means of the type I seesaw. The model predicts an inverse mass hierarchy, a massless neutrino and a vanishing reactor neutrino mixing angle nowadays ruled out [2].

2 Reactor mixing angle and the DDM mechanism

We consider two extensions (model A and B) of the original DDM model, where we have added one extra RH neutrino N_5, as $\mathbf{1}'$ in model A and $\mathbf{1}''$ in model B, and three real scalar singlets of the SM as the triplet $\phi = (\phi_1,\ \phi_2,\ \phi_3)$. The relevant particle content is summarised on Tables 1 and 2. The flavon fields ϕ acquire a vev around the seesaw scale, such that A_4 is broken into Z_2 at this scale, contributing to the RH neutrino masses.

Model A

	L_e	L_μ	L_τ	l_e^c	l_μ^c	l_τ^c	N_T	N_4	N_5	H	η	ϕ
SU(2)	2	2	2	1	1	1	1	1	1	2	2	1
A_4	1	$1'$	$1''$	1	$1''$	$1'$	3	1	$1'$	1	3	3

Table 1: *Summary of the relevant particle content for model A.*

Considering the matter content in Tab. 1, the relevant part of the Lagrangian is given by[1 2]:

$$\mathcal{L}_{\rm Y}^{(\rm A)} = y_1^\nu L_e [N_T\,\eta]_1 + y_2^\nu L_\mu [N_T\,\eta]_{1''} + y_3^\nu L_\tau [N_T\,\eta]_{1'} + y_4^\nu L_e\, N_4\, H$$
$$+ y_5^\nu L_\tau\, N_5\, H \ + M_1\, N_T N_T + M_2\, N_4 N_4 \tag{1}$$
$$+ y_1^N [N_T\,\phi]_3 N_T + y_2^N [N_T\,\phi]_1 N_4 + y_3^N [N_T\,\phi]_{1''} N_5 + h.c.$$

In this way H is responsible for the quarks and charged lepton masses, the latter automatically diagonal. The Dirac neutrino mass matrix arises from H and η, and the flavon fields will contribute to the RH neutrino mass matrix. In order to preserve a Z_2 symmetry, the alignment of the vev's take the form:

$$\langle H^0 \rangle = v_h \neq 0,\ \ \langle \eta_1^0 \rangle = v_\eta \neq 0,\ \ \langle \eta_{2,3}^0 \rangle = 0,\ \ \langle \phi_1 \rangle = v_\phi \neq 0,\ \ \langle \phi_{2,3} \rangle = 0. \tag{2}$$

From Eqs. (1) and (2) the light neutrinos get Majorana masses through the type-I seesaw relation taking the form:

$$m_\nu^{(\rm A)} \equiv \begin{pmatrix} a & 0 & b \\ 0 & 0 & c \\ b & c & d \end{pmatrix}, \tag{3}$$

with $a = \frac{(y_4^\nu v_h)^2}{M_2}$, $b = \frac{y_1^\nu y_5^\nu v_\eta v_h}{y_3^N v_\phi} - \frac{y_2^N y_4^\nu y_5^\nu v_h^2}{y_3^N M_2}$, $c = \frac{y_2^\nu y_5^\nu v_\eta v_h}{y_3^N v_\phi}$, and $d = \frac{(y_2^N y_5^\nu v_h)^2}{(y_3^N)^2 M_2} - \frac{(y_5^\nu v_h)^2 M_1}{(y_3^N v_\phi)^2} + 2\ \frac{y_3^\nu y_5^\nu v_\eta v_h}{y_3^N v_\phi}$. This has the B_3 two-zero texture 3) and is consistent with both neutrino mass hierarchies and can accommodate the experimental value for the reactor mixing angle, θ_{13} 4).

Model B

	L_e	L_μ	L_τ	l_e^c	l_μ^c	l_τ^c	N_T	N_4	N_5	H	η	ϕ
SU(2)	2	2	2	1	1	1	1	1	1	2	2	1
A_4	1	$1'$	$1''$	1	$1''$	$1'$	3	1	$1''$	1	3	3

Table 2: *Summary of the relevant particle content for model B.*

[1] The term $y_1^N [N_T\,\phi]_3 N_T$ accounts for the symmetric part of $[N_T\,\phi]_{3_1}$ and $[N_T\,\phi]_{3_2}$.

[2] $[a,\,b]_j$ stands for the product of the two triplets a, b are contracted into the j representation of A_4

The relevant part of the Lagrangian for model B, Tab. 2, is given by

$$\begin{aligned}\mathcal{L}_{\rm Y}^{(\rm B)} &= y_1^\nu L_e [N_T\,\eta]_1 + y_2^\nu L_\mu [N_T\,\eta]_{1''} + y_3^\nu L_\tau [N_T\,\eta]_{1'} + y_4^\nu L_e\, N_4\, H \\ &+ y_5^\nu L_\mu\, N_5\, H + M_1\, N_T N_T + M_2\, N_4 N_4 \\ &+ y_1^N [N_T\,\phi]_3 N_T + y_2^N [N_T\,\phi]_1 N_4 + y_3^N [N_T\,\phi]_{1'} N_5 + h.c.\end{aligned} \tag{4}$$

The mass matrix of the charged leptons is diagonal, while the light neutrinos Majorana mass matrix after the type I seesaw is

$$m_\nu^{(\rm B)} \equiv \begin{pmatrix} a & b & 0 \\ b & d & c \\ 0 & c & 0 \end{pmatrix}, \tag{5}$$

with a and b as in model A and $c = \frac{y_3^\nu y_5^\nu v_\eta v_h}{y_3^N v_\phi}$, and $d = \frac{(y_2^N y_5^\nu v_h)^2}{(y_3^N)^2 M_2} - \frac{(y_5^\nu v_h)^2 M_1}{(y_3^N v_\phi)^2} + 2\,\frac{y_2^\nu y_5^\nu v_\eta v_h}{y_3^N v_\phi}$. This correspond to the two-zero texture mass matrix B_4 [3], which is also consistent with both neutrino mass hierarchies and can also accommodate the reactor mixing angle.

3 Results

We performed the analysis using four independent constraints, coming from the two complex zeroes, to correlate two of the neutrino mixing parameters. We took the experimental values, using data from [5], as inputs and numerically scanned within their 3σ regions and determine the regions allowed by two correlated variables of interest.

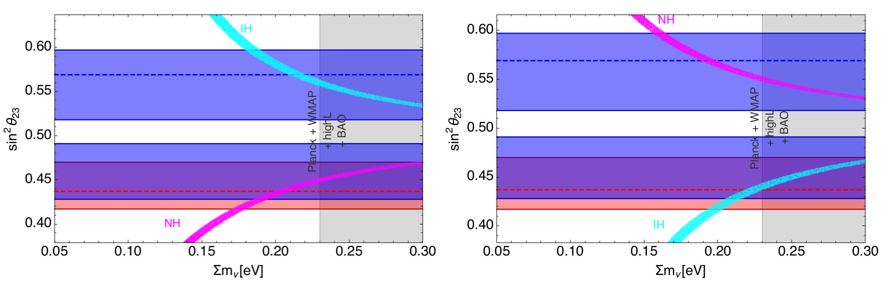

Figure 1: Correlation between $\sin^2\theta_{23}$ and the sum of the light neutrino masses, $\sum m_\nu$, see text for description.

In Fig. 1 we show the correlation between the atmospheric mixing angle, $\sin^2\theta_{23}$, and the sum of light neutrino masses, $\sum m_\nu$, for model A (B) on the left (right). In the graphics, the allowed 3σ regions in $\sin^2\theta_{23}$ vs. $\sum m_\nu$, for the normal hierarchy (NH) is plotted in magenta and for the inverse hierarchy (IH) in cyan. The 1σ in the atmospheric angle is represented by the horizontal blue (red) shaded regions for the IH (NH) and the best fit values correspond to the horizontal blue (red) dashed lines for the IH (NH). The grey vertical band represents a disfavoured region in neutrino masses [6]. Fig. 1 also shows that in model A both hierarchies have an overlap with the 1σ region for $\sin^2\theta_{23}$, while in model B only in the IH case has such overlap in the second octant.

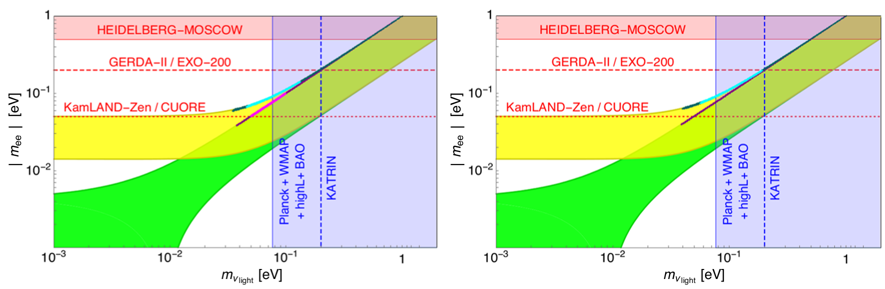

Figure 2: Effective $0\nu\beta\beta$ parameter $|m_{ee}|$ versus the lightest neutrino mass $m_{\nu_{\rm light}}$, see text for description.

The Fig. 2 shows $m_{\nu_{\rm light}}$ vs. $|m_{ee}|$ for model A (B) on the left (right). The region for the NH (IH) within 3σ in $\sin^2\theta_{23}$ are in dark magenta (dark cyan) and the overlap for 1σ in magenta (cyan). The red (blue) shaded region corresponds the current experimental limits [6, 7]. The yellow (green) the bands correspond to the 3σ "flavor-generic" IH (NH) spectra. The Fig. 2 also shows that the results in model B do not overlap with the 1σ region for NH case. The models predict Majorana phases giving a minimal cancellation for the $|m_{ee}|$. Both two-zero textures are sensitive to the value of the atmospheric mixing angle that is translated as the localised region for neutrinoless double beta decay effective parameter within the near future experimental sensitivity.

4 Conclusions

We have constructed two models based on the DDM mechanism where the A_4 is spontaneously broken at the seesaw scale, into a remanent Z_2. The models have two Z_2 odd and three Z_2 even RH neutrinos, the latter giving light neutrino masses via type-I seesaw. The breaking of A_4 is leaded by the flavon fields in a way that we get two-zero textures for the light Majorana neutrinos mass matrices. These are in agreement with the experimental data and both mass hierarchies. The models also contain a DM candidate stabilised by Z_2 symmetry. Finally, we have presented correlations between mixing parameters and lower bounds for neutrinoless double beta regions.

ACKNOWLEDGEMENTS

I wuold like to thank my collaborator E. Peinado for the work presented here and the organisers of the 5th Young Researchers Workshop: "Physics Challenges in the LHC Era" for the invitation. This work was possible thanks to the grant No. PAPIIT IA101516 and CONACyT.

References

1. M. Hirsch, S. Morisi, E. Peinado and J. W. F. Valle, Phys. Rev. D **82** (2010) 116003 doi:10.1103/PhysRevD.82.116003 [arXiv:1007.0871 [hep-ph]].

2. W. Tang [Daya Bay Collaboration], arXiv:1512.00335 [hep-ex].

3. P. H. Frampton, S. L. Glashow and D. Marfatia, Phys. Lett. B **536** (2002) 79 doi:10.1016/S0370-2693(02)01817-8 [hep-ph/0201008].

4. D. Meloni, A. Meroni and E. Peinado, Phys. Rev. D **89**, no. 5, 053009 (2014) doi:10.1103/PhysRevD.89.053009 [arXiv:1401.3207 [hep-ph]].

5. F. Capozzi, E. Lisi, A. Marrone, D. Montanino and A. Palazzo, arXiv:1601.07777 [hep-ph].

6. P. A. R. Ade *et al.* [Planck Collaboration], arXiv:1502.01589 [astro-ph.CO].

7. V. E. Guiseppe *et al.* [Majorana Collaboration], arXiv:0811.2446 [nucl-ex]; M. Agostini *et al.* [GERDA Collaboration], Phys. Rev. Lett. **111** (2013) 12, 122503, [arXiv:1307.4720 [nucl-ex]]; J. B. Albert *et al.* [EXO-200 Collaboration], Nature **510** (2014) 229, [arXiv:1402.6956 [nucl-ex]]; A. Gando *et al.* [KamLAND-Zen Collaboration], Phys. Rev. Lett. **110** (2013) 6, 062502, [arXiv:1211.3863 [hep-ex]]; A. Giuliani [CUORE] , Journal of Physics: Conference Series **J** 120 (2008), 052051; L. Bornschein [KATRIN Collaboration], eConf C **030626** (2003) FRAP14, [hep-ex/0309007].

A no-go theorem for the dark matter interpretation of the positron anomaly

Maxim Laletin
Space sciences, Technologies and Astrophysics Research (STAR) Institute
Université de Liège, Bât B5A, Sart Tilman, 4000 Liège, Belgium
and
National Research Nuclear University MEPhI,
115409 Kashirskoe shosse 31, Moscow, Russia

Abstract

The overabundance of high-energy cosmic positrons, observed by PAMELA and AMS-02, can be considered as the consequence of dark matter decays or annihilations. We show that recent FERMI/LAT measurements of the isotropic diffuse gamma-ray background impose severe constraints on dark matter explanations and make them practically inconsistent.

1 Introduction

The unexpected increase of the positron fraction in cosmic rays with energies above 10 GeV (also known as the "positron anomaly") was observed for the first time in the PAMELA experiment [2] and was later confirmed by AMS-02 [3]. A lot of attention was paid to this discovery since the standard mechanisms of positron production and acceleration predicted a much steeper energy spectrum of cosmic positrons. The list of possible explanations includes, inter alia, decays or annihilations of dark matter (DM) particles, implying the existence of interconnection between our world and "dark world". This intriguing possibility is though highly constrained by a set of direct, indirect and accelerator-based observations, which force DM models to become more and more sophisticated. But no matter how complicated a DM model explaining the positron anomaly is, it should obviously fulfill the principal requirement that it produces a sufficient amount of high-energy positrons. The undesirable consequence of this fact is that, regardless of the prior (internal) processes, production of charged particles is accompanied by gamma-ray emission (see Fig. 1).

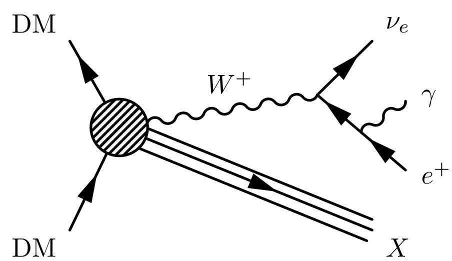

Figure 1: A diagram illustrating an example of the DM annihilation process providing a positron via W^+ decay and some variety of states X. The positron emits final state radiation (FSR).

In addition, gamma rays are produced during the propagation of charged particles through the Galactic gas and the electromagnetic media, mainly in such processes as Bremsstrahlung and inverse Compton scattering (ICS). As we are going to show, even this at first sight small contribution to Galactic gamma rays may come in conflict with the latest Fermi-LAT data on the isotropic diffuse gamma-ray background [4, 5] and, furthermore, rule out DM explanations of the high-energy cosmic positron excess. Basically, the reason of this problem is the following: the total amount of positrons and photons depends on the size of the volume in which their sources are concentrated, and though physically both positrons and photons have the same source, the volume of space from which they mostly arrive is substantially different. While only those positrons that were produced in the ~ 3 kpc proximity can approach the Earth (due to their stochastic motion in the Galactic magnetic fields and the corresponding energy losses), gamma rays can come to us directly from any point of the DM halo, where they were born. Now, since the DM halo is indeed large, the amount of gamma rays can simply overwhelm the observed limits.

2 The theorem

The no-go theorem we are considering can be expressed as follows:

Any model of DM providing a satisfactory explanation of the high-energy cosmic positron data and assuming an isotropic distribution of annihilating or decaying DM particles in the Galactic halo produces an overabundance of gamma rays that contradicts the latest experimental data on the diffuse gamma-ray background.

The proof starts with "the extraction" of the initial (injection) spectrum of positrons produced in DM annihilations from the cosmic positron data (decays result in larger values of gamma-positron ratio compared to the case of annihilations and hence are discarded right away). Though, technically we did it the other way round (see [1]) for the details) – we found the injection spectrum, which eventually (after taking into account the effects of propagation) provides the best possible fit to the AMS-02 data on cosmic positron fraction (Fig. 2).

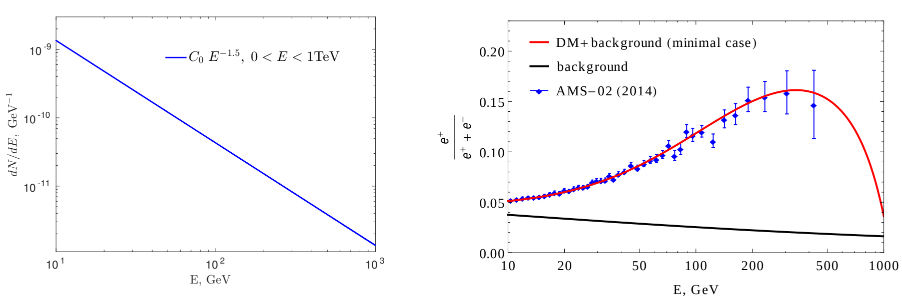

Figure 2: DM positron injection spectra (left), providing the best possible fit to the AMS-02 positron fraction data (right).

To calculate the local fluxes of positrons (and the ICS and Bremsstrahlung contributions to gamma rays) from DM annihilations, the GALPROP code was used [6]. One may argue that our results depend on the choice of propagation parameters (spatial diffusion coefficient, size of magnetic halo, etc.), which are not really well defined yet (we used the set of propagation parameters providing the best fit of AMS-02 proton and Boron-to-Carbon data [7]). We agree that a piece of uncertainty comes from the propagation model, though we do not expect it to influence the result significantly. In other words, a “finely tuned” propagation model is not likely to solve the problem with gamma rays.

Now, we want to estimate the “minimal” model-independent initial spectra of prompt gamma radiation. In these estimations we concentrate on the fact that the positron with a given energy was produced in an elementary process, which appears as some part of the DM annihilation cascade. For example, this process might be a W^+ or Z decay or even the decay of some new positively charged massive particle. The set of possible vertices is, first of all, limited by Lorentz symmetry and renormalizability of the interaction. Thus, at the tree level, we are left with four point vertices (Fig. 3).

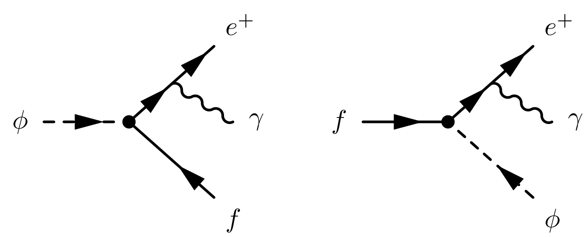

Figure 3: The diagramms illustrating two allowed types of elementary processes providing a positron in the final state. Here f denotes any fermion enabled by the symmetry group and kinematics and ϕ any enabled integer spin field.

Since we are interested in positrons and gamma rays with energies above 10 GeV, we expect that the energy spectrum of final state radiation from e^+ would only depend on the energy of the emitting positrons and that it can be calculated as

$$\frac{dN}{dE} = \int\limits_{E}^{1\ \mathrm{TeV}} \phi_\gamma(E, E_0) f_e(E_0)\, dE_0, \tag{1}$$

where $f_e(E_0)$ denotes the initial spectrum of positrons (see Fig. 2) and $\phi_\gamma(E, E_0)$ denotes the spectrum of photons produced by the positrons with energy E_0. It is given by [8]

$$\phi_\gamma(E, E_0) = \frac{\alpha}{\pi E}\left(1 + \left(1 - \frac{E}{E_0}\right)^2\right)\left(\ln\left[\left(\frac{2E_0}{m_e}\right)^2\left(1 - \frac{E}{E_0}\right)\right] - 1\right). \quad (2)$$

Here we neglect the difference in the positron spectra *before* and *after* photon emission. The resulting minimal flux of gamma rays from DM annihilations is shown in Fig. 4.

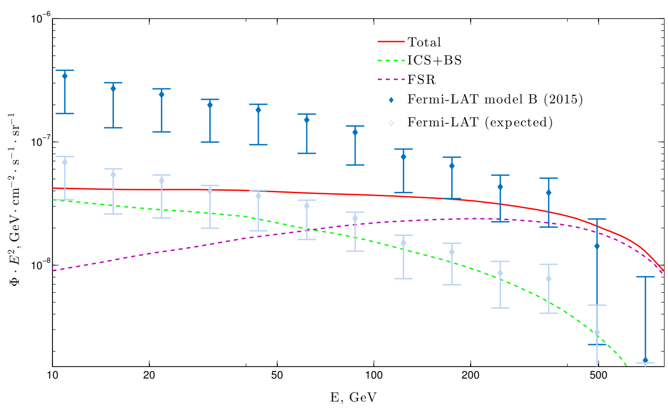

Figure 4: The minimal gamma ray flux from DM annihilations compared to the contemporary [4] and expected [5] Fermi-LAT data on IGRB. Two major contributions are shown separately in different colors.

As one can see, the minimal gamma-ray flux obtained satisfies the contemporary Fermi-LAT limit (except the last data point, which has a large error though), but, according to one of their recent papers [5], more than 80% of IGRB can be explained by unresolved astrophysical sources, such as active galactic nuclei. This new (expected) limit turns out to be much lower than the predicted minimal flux of gamma rays. *Q.E.D.*

Also, one should take into account two facts, which make our result even stronger: a) we didn't take into consideration the extragalactic gamma-ray flux (since its estimations are model-dependent), which may be comparable to the Galactic one; b) practically, any DM model yields more prompt radiation than just the contribution from positrons.

One of the key assumptions of our theorem is the conventional isotropic distribution of annihilating/decaying DM. As it was shown in one of our works [1) one can circumvent this no-go theorem by assuming a non-isotropic positron source distribution, e.g. a dark matter disk.

Acknowledgments

The author thanks all the co-authors of the original article for their valuable contributions: K. Belotsky, R. Budaev and A. Kirillov. I thank J.-R. Cudell for his ideas, inspiring this research. I am also grateful to A. Bhattacharya, M. Khlopov and D. Wegman for fruitful discussions. This work is supported by a FRIA grant (F.N.R.S.).

References

1. These proceedings are based on the following article:
   K. Belotsky, R. Budaev, A. Kirillov, and M. Laletin, (2016), 1606.01271.
2. PAMELA, O. Adriani *et al.*, Nature **458**, 607 (2009), 0810.4995.
3. AMS, M. Aguilar *et al.*, Phys. Rev. Lett. **110**, 141102 (2013).
4. Fermi-LAT, M. Ackermann *et al.*, Astrophys. J. **799**, 86 (2015), 1410.3696.
5. Fermi-LAT, M. Di Mauro, The origin of the Fermi-LAT γ-ray background, in *Proceeding of the MG14 conference*, 2016, 1601.04323.
6. The GALPROP code for cosmic-ray transport and diffuse emission production, http://galprop.stanford.edu/.
7. H.-B. Jin, Y.-L. Wu, and Y.-F. Zhou, JCAP **1509**, 049 (2015), 1410.0171.
8. R. Essig, N. Sehgal, and L. E. Strigari, Phys. Rev. **D80**, 023506 (2009), 0902.4750.

Light Dark Matter with AURIGA detector

Antonio Branca
INFN of Padova, Padova, Italy

Abstract

The search power of the cryogenic resonant-mass AURIGA detector for a new scalar field called moduli, has been explored in the present work. Moduli are predicted by String Theory and may have significant contribution to the Dark Matter in our universe. Interactions of moduli with ordinary matter causes the oscillation of solids with a frequency equal to the moduli mass. Thus, the AURIGA detector could detect moduli as a resonance within its bandwidth. In the following, the signal characteristics have been studied through simulation and a projection of the sensitivity has been obtained.

1 Introduction

Dark Matter (DM) might be made of light particles, with respect to the masses of particles involved in the Standard Model (SM). A good candidate for DM in this case are the so called moduli (Φ), scalar fields predicted by String

Theory, with light mass (m_Φ) values depending on the considered model. From a phenomenological point of view, the moduli mass has to be heavier than $m_\Phi \simeq 10^{-22}\,eV$, in order for these particles to cluster through gravitational effects at galactic scales and form the so called DM galactic-halo. Assuming the standard DM model, with an energy density in our galaxy of $\rho_{DM} = 0.3\,GeV/cm^3$, if the moduli mass is lighter than $m_\Phi \simeq 0.1\,eV$, the number of occupancy of moduli is high, and they can be described with a classical wave thanks to the correspondence principle. In this case, the interaction of ordinary matter with the DM halo, causes the mass of electrons, m_e, and the fine structure constant, α, to oscillate in time. This implies an oscillation of the atoms size in matter, causing an oscillation of the size of a given solid. This effect has been pointed out and thoroughly studied in the paper [1]. As reported in this paper, a search of such effect on matter can be already performed by exploiting existing resonant-mass detectors, which were built for gravitational waves detection.

2 Effects on ordinary matter

Moduli interact with SM particles and in particular, for the purpose of this discussion, with electrons and photons:

$$\mathcal{L}_\Phi^{\mathrm{int}} \supset \sqrt{4\pi \mathrm{G_N}}\Phi \left[\mathrm{d_{m_e} m_e e\bar{e}} - \frac{\mathrm{d_e}}{4}\mathrm{F}_{\mu\nu}\mathrm{F}^{\mu\nu}\right]$$

where d_{m_e} and d_e are the moduli coupling to the electron field, e, and electromagnetic field strength $F_{\mu\nu}$, respectively. The coupling to the electromagnetic field modifies the Maxwell Lagrangian, and the moduli field is absorbed by the fine structure constant α:

$$\alpha(\mathbf{x}, t) = \alpha(1 + d_e\sqrt{4\pi G_N}\Phi(\mathbf{x},t)) \tag{1}$$

Wherease, the coupling to the electron field modifies the electron mass term, with the moduli field absorbed in the electron mass:

$$m_e(\mathbf{x}, \mathrm{t}) = m_e(1 + d_{m_e}\sqrt{4\pi G_N}\Phi(\mathbf{x}, \mathrm{t})) \tag{2}$$

Since the moduli field can be described by a classical wave:

$$\Phi(\mathbf{x}, \mathrm{t}) = \Phi_0 cos(m_\Phi t - m_\Phi \mathbf{v}\cdot\mathbf{x}) + O(v^2)$$

then the two constants (1) and (2) oscillate in time around their nominal values along with the moduli field. This implies the oscillation of the atom's size, $a_0 \propto 1/\alpha m_e$, with a relative deformation with respect to their nominal size of:

$$h \equiv \frac{\delta a_0}{a_0} = -(d_e + d_{m_e})\sqrt{4\pi G_N}\Phi(\mathbf{x}, \mathrm{t}) \tag{3}$$

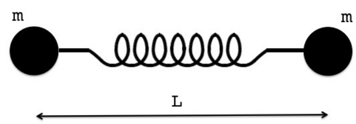

Figure 1: Simple oscillator model: two mass points m connected by a real spring with elastic constant k and equilibrium length L.

3 Effects on an oscillator

We focus now on the macroscopic effect of moduli on a body of size L and mass M. As a naive approximation, we may consider the body as made of two mass points, each one of mass $m = M/2$, connected by a real dissipative spring of elastic constant k and equilibrium length L (fig. 1):

If x is the relative position of the two masses, then the equation of motion for the oscillator is:

$$\ddot{x} + \frac{\omega}{Q}\dot{x} + \omega^2(x - L) = F_{ext} + F_{th} \tag{4}$$

where $\omega = \sqrt{k/m}$ is the characteristic angular frequency, Q the quality factor and $F_{ext/th}$ the external/thermal force acting on the oscillator. The effect of moduli field is such that it changes the equilibrium position L, and it is evident in equation (4) once we write it in terms of the displacement, $\xi = x - L$, taking into account that $\ddot{x} = \ddot{\xi} + \ddot{\delta L} = \ddot{\xi} + \ddot{h}L$:

$$\ddot{\xi} + \frac{\omega}{Q}\dot{\xi} + \omega^2\xi = -\ddot{h}L + F_{ext} + F_{th} \tag{5}$$

Eq. (5) is similar to the one of a resonant detector for gravitational waves (GW), subject to a GW tidal force. The term $F_\Phi = -\ddot{h}L$ can be interpreted as the corresponding force acting on the oscillator due to moduli field, differing with respect to the GW tidal force just for a 1/2 factor. Given this result, we are allowed to exploit the resonant mass experiments for GW detection already in place to search for moduli.

4 The AURIGA detector

AURIGA represents the state-of-art in the class of gravitational wave cryogenic resonant-mass detectors. It is located at INFN National Laboratory of Legnaro (Italy) and has been in continuous operation from year 2004. The read-out scheme of the detector is shown in fig. 2

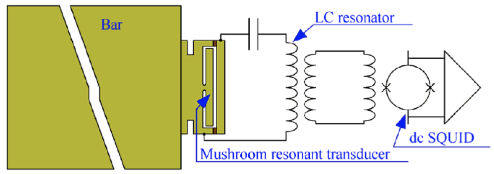

Figure 2: Scheme of the read-out of AURIGA detector (see text).

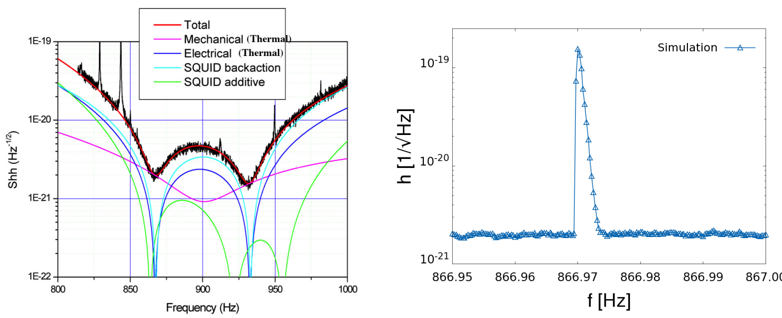

Figure 3: (color online) [*left*] measured noise power spectrum (black-curve) of AURIGA detector compared to the prediction (red-curve) from Fluctuation-Dissipation Theorem. The breakdown of the different noise contribution is also shown. [*right*] Simulation of a moduli signal with coupling $(d_{m_e} + d_e) = 5 \cdot 10^{-4}$ and frequency $f_\Phi \simeq 867\,Hz$ plus white noise with standard deviation $\sigma = 2 \cdot 10^{-21} 1/\sqrt{Hz}$. The signal is a narrow peak with a bandwidth of $\triangle f \simeq 1\,mHz$.

The system is made of three coupled resonators with nearly the same resonant frequency $f_R \sim 900\,Hz$. The detector core is a cylindrical bar of aluminium alloy, cooled to liquid helium temperatures. Moduli would affect the size of the bar making its fundamental longitudinal mode resonate. The mechanical energy is then transfered to a mashroom-shaped resonator, attached to one of the end faces of the cylinder. This additional resonator amplifies the mechanical energy of the signal and transduces it into an electrical signal. The latter is further amplified through a LC resonator and picked up by a squid amplifier. The detector is a system in thermal equilibrium, then its thermal noise fluctuation are described by the Fluctuation-Dissipation Theorem. The measured noise power spectrum is shown in fig. 3-left: we can see a good agreement between data and prediction.

The sensitivity, set by the thermal noise in fig. 3-left, is $h \simeq 2 \cdot 10^{-21}\, 1/\sqrt{Hz}$

within a factor of 2 over a bandwidth of $\triangle f \simeq 100\,Hz$.

5 Predicted AURIGA sensitivity

To compute the power spectrum of the strain in eq. (3), we use the so called Standard Halo Model (SHM) that assumes a spherical DM halo for the Galaxy with local DM density of $\rho_{DM} = 0.3\,GeV/cm^3$, and an isotropic Maxwell-Boltzmann speed distribution [2]. In this framework, if moduli make up the DM in our Universe then the corresponding field $\Phi(\mathbf{x}, \mathrm{t})$ can be scribed as a zero mean stochastic process with a Maxwell-Boltzmann power spectrum density [3], consequently the spectrum of the relative deformation h is given by:

$$h(f) = 1.5 \times 10^{-16} \frac{(d_{m_e} + d_e)}{a^{\frac{3}{4}} f_\Phi} (|f| - f_\Phi)^{\frac{1}{4}} e^{-\frac{(|f|-f_\Phi)}{2a}} \Theta(|f| - f_\Phi) \left[\frac{1}{\sqrt{Hz}}\right] \quad (6)$$

where f_Φ is the frequency corresponding to moduli with a given mass, $a = 1/3 f_\Phi \left\langle v^2 \right\rangle$ and $v^2/c^2 \sim 10^{-6}$ the mean squared velocity of DM halo. A strain with square root power spectrum density given by this equation can be detected by the high sensitive resonant-mass AURIGA detector, by analyzing the noise power spectrum $P(f)$ of the read-out output. The power spectrum, once it is calibrated, $P^{cal}(f)$, gives the information on the strain of the bar:

$$h^2 = \int_{\triangle f} P^{cal}(f) df \quad (7)$$

A simulation of the detector response is made to study the properties of the DM signal. The simulated signal frequency is chosen to lie in one of the two regions where AURIGA detector has the best sensitivity, has can be seen in fig. 3-left, specificaly $f_\Phi \simeq 867\,Hz$. From eq. (6) is already evident the narrow bandwidth of the considered signal. For this reason, we may assume the noise to be white, $\langle n_i \rangle = 0$, $\langle n_i n_j \rangle = \sigma^2 \delta_{ij}$, around the signal peak, with a standard deviation of $\sigma = 2 \cdot 10^{-21} 1/\sqrt{Hz}$, equal to the noise level at $f_\Phi \simeq 867\,Hz$. The simulated signal strength is set by the chosen value for the coupling to ordinary matter of $(d_{m_e} + d_e) = 5 \cdot 10^{-4}$. The simulation result is shown in fig. 3-right.

The expected signal (6) has a bandwidth of about $\triangle f \simeq 1\,mHz$ in the sensitive band of AURIGA. Supposing we have a given dataset to be analyzed, a proper spectrum resolution to spot such a narrow signal is achieved by splitting the dataset into one hour long data streams and performing power spectrum computation on each stream. A reduction of the noise standard deviation of each spectrum is achieved by computing the average of all the spectrums, resulting in a gain in sensitivity. If N is the number of averaged power spectrums, the standard deviation of the noise is $N^{1/2}$ [4]. Given eq. 7, the corresponding standard deviation on h decreases with the number of averages as $N^{1/4}$. Thus, a sensitivity plateau on the moduli signal is already achieved with few weeks of data. Eventually, the predicted sensitivity of the AURIGA detector to a moduli signal can be estimated by:

$$S_\Phi = \frac{1}{2} h_{GW} \cdot \triangle f^{1/2} \cdot N^{-1/4} \tag{8}$$

where h_{GW} is the sensitivity to the GW shown in fig. 3-left and 1/2 is due to the factor 2 difference in the signal from a GW and the one from DM moduli. Also, we have to take into account that the signal has a width $\triangle f$, smearing the signal power spectrum and thus worsening the sensitivity by a factor of $\triangle f^{1/2}$; finally, a gain of $N^{1/4}$ in sensitivity is obtained by averaging N power spectrum. Assuming a dataset one month long, the total number of power spectrum can be computed on one hour long data stream is $N \simeq 700$. The sensitivity which can be reached at $f = 867\,Hz$, from eq. 8, is then $S_\Phi \simeq 6 \cdot 10^{-24}$. By using eg. 6, the corresponding sensitivity on the coupling of moduli to matter that can be reached is $(d_{m_e} + d_e) \lesssim 3.5 \times 10^{-5}$, with respect to the gravitational force strength. This is in the interesting physical region, as shown by the paper [1].

References

1. A. Arvanitaki, S. Dimopoulos, K. V. Tilburg, Phys. Rev. Lett. 116, 031102 (2016).

2. J. D. Lewin and P. F. Smith, Astropart. Phys. 6 (1996) 87.

3. L. Krauss, J. Moody, F. Wilczek, D. E. Morris, Phys. Rev. Lett. **55**, 1797 (1985).

4. D. G. Manolakis, J. G. Proakis, Digital Signal Processing: principles, algorithms and applications, 3rd ed. (Upper Saddle River: Prentice-Hall, c1996), Chap. 12, p. 908.

The PADME experiment at Laboratori Nazionali di Frascati

Gabriele Piperno for the PADME collaboration
Laboratori Nazionali di Frascati, Frascati, Italy

Abstract

The PADME experiment will search for the invisible decay of Dark Photons produced in interactions of positron from the DAΦNE Linac on a target. The collaboration aims at reaching a sensitivity of $\sim 10^{-3}$ on the coupling constant for values of Dark Photon masses up to 23.7 MeV.

1 Introduction

The problem of the elusiveness of the Dark Matter (DM) can be solved speculating that it interacts with particles and gauge fields of the Standard Model (SM) only by means of portals that connect our world to the dark sector. The simplest model adds a U(1) symmetry and its vector boson A': SM particles are neutral under this symmetry, while the new boson couples to the SM with an effective charge εe and for this reason it is called Dark Photon (DP). [1, 2]

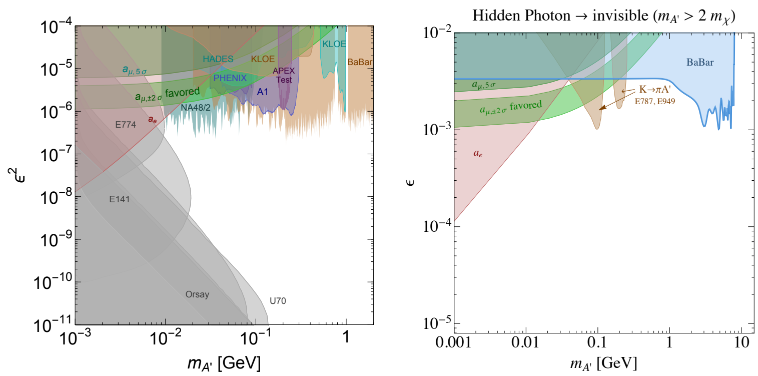

Figure 1: Current DP search status: on the left for visible decays (adapted from [4]), on the right for the invisible ones (adapted from [5]). Typical DP exclusion plot have the A' mass on the x-axis and the coupling constant (squared) on the y-axis. In both cases the 2σ anomalous muon magnetic moment favored band is indicated.

In addition, it has been pointed that the existence of an A' with a mass $m_{A'}$ in the range $[1\,\mathrm{MeV}, 1\,\mathrm{GeV}]$ and a coupling constant $\varepsilon \sim 10^{-3}$, might be responsible for the discrepancy currently observed between the theoretical expectation, based on the SM, and the measurement of the muon anomalous magnetic moment $(g-2)_\mu$. [3]

If there are no particles in the hidden sector with mass smaller than one half of A', it can only have SM decays (visible decays). Currently, the region of the ε, $m_{A'}$ plane favored by $(g-2)_\mu$ discrepancy, is excluded for an A' decaying into SM (see Fig.1 left).

In the most general case the A' can decay into DM (invisible decays). In this scenario, there are still unexplored regions in the $(g-2)_\mu$ favored band, as shown in Fig.1 right.

A comprehensive overview of the experimental programs of this field is presented in [6].

2 The PADME experiment

The PADME (Positron Annihilation into Dark Mediator Experiment) experiment is designed to detect invisible decaying DPs that are produced in the reaction $e^+ e^- \rightarrow A' \gamma$, where the e^+ are accelerated from the DAΦNE to 550 MeV and the e^- belongs to a fixed target. [7, 8]

2.1 The Frascati Beam Test Facility

PADME will be hosted in the newly redesigned hall of the Beam Test Facility (BTF), a transfer-line from the DAΦNE linac of the Laboratori Nazionali di Frascati (LNF). [9] BTF is able to provide up to 50 bunches/s with a maximum energy of 550 and 800 MeV, for positrons and electrons respectively, and with duration (at constant intensity) from 1.5 to 40 ns. The energy spread is 0.5%, while the beam spot size can vary by orders of magnitude: $[0.5, 25]$ mm (vertical) $\times$ $[0.6, 55]$ mm (horizontal). The number of particles that can be provided per bunch goes from 1 to 10^{10}.

2.2 The detector

The detector is designed to identify events with a single photon emerging from the e^+/e^- annhilation and to measure the missing squared invariant mass of the final state, by exploiting energy-momentum conservation and the fully constrained initial state: e^+ beam (known momentum and position) on an active fixed target. The A' squared invariant mass M^2_{miss} can be estimated as:

$$M^2_{miss} = \left(\vec{P}_{e^-} + \vec{P}_{beam} - \vec{P}_{\gamma}\right)^2 ,$$

where $\vec{P}_{e^-} = \vec{0}$ and $P_{beam} = 550\,\mathrm{MeV}$ along the initial beam direction, are the e^- and the e^+ momentum respectively and $\vec{P}_{\gamma}$ is the photon final state.

The detector, shown Fig.2, consists of different components: [7]

- Diamond active target. It allows to measure the beam intensity and position (precision of ≈ 5 mm) by means of graphite perpendicular strips. The low Z of diamond is needed to reduce the bremsstrahlung process. The area is $2 \times 2\,\mathrm{cm}^2$ and the small thickness ($50\,\mu$m or $100\,\mu$m) is to reduce the probability of e^+ multiple interactions.

- Dipole magnet. Located 20 cm after the target, it is designed to deflect exhaust beam out of the detector and send the positrons that lost part of their energy (mainly through bremsstrahlung) towards the vetoes. The field is 0.5 T over a gap of 23 cm for 1 m of length.

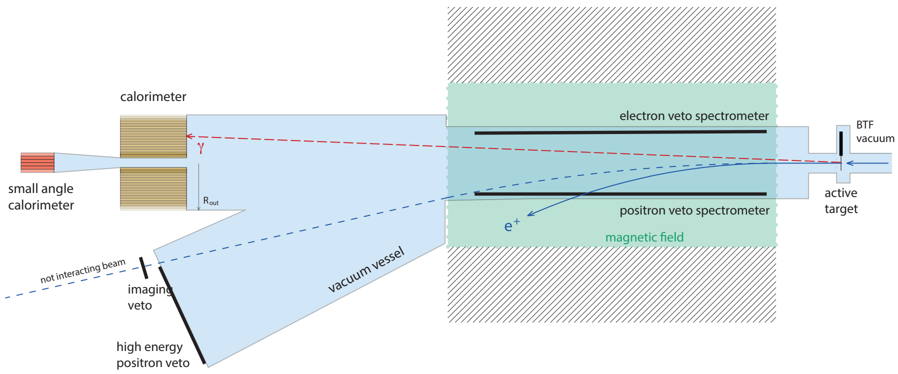

Figure 2: PADME detector layout. From right to left: the active target, the e^+e^- vetoes inside the magnetic dipole, the high energy e^+ veto near the exhaust beam exit, the ECAL and the SAC. The distance between the ECAL and the target is 3 m.

- Positrons/electrons veto. It is divided into two parts: one inside the dipole for positrons and electrons and one, near the beam exit, for high energy positrons that lost only a small part of their energy, typically for bremsstrahlung. It is composed of $1 \times 1 \times 16\,\mathrm{cm}^3$ bars of plastic scintillators. The arrays inside the magnet are ≈ 1 m long, while the high energy positron one is ≈ 0.5 m long.

- Electromagnetic calorimeter (ECAL). Made of 616 $2 \times 2 \times 22\,\mathrm{cm}^3$ BGO crystals and placed at 3 m from the target. Energy resolution is foreseen to be $\sim \frac{(1-2)\%}{\sqrt{E}}$. The shape is cylindrical (30 cm radius) with a central hole (a square of 10 cm side) to allow the bremsstrahlung radiation to pass and impinge on the Small Angle Calorimeter. This is necessary because of the BGO decay time of 300 ns: the ECAL would be continuously "blinded" by the bremsstrahlung rate. The angular coverage is $(20, 93)$ mrad.

- Small Angle Calorimeter (SAC). It consists of 49 $2 \times 2 \times 20\,\mathrm{cm}^3$ lead glass SF57 and its goal is to veto events with a bremsstrahlung photon. The lead glass decay time of 4 ns makes it a good candidate for this task, being fast enough for the expected rate. The angular coverage is $(0, 20)$ mrad.

Hence the DP signature is a single γ in the ECAL and no particles in the vetoes. Being $E_{beam} = 550$ MeV, the largest A' reachable mass is 23.7 MeV.

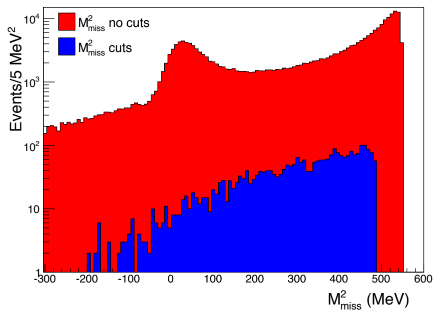

Figure 3: Background before (red) and after (blue) good events selection.

2.3 Backgrounds and sensitivity

The SM physical processes that take place when the e^+ beam hits the target are: bremsstrahlung and e^+/e^- annihilation in 2 or 3 γs. [7] The probability that they mimic a DP production event can be reduced through an optimization of the ECAL geometry and granularity and of the system of vetoes. The beam intensity plays an important role through the pileup: clusters cannot be resolved in time by the calorimeter if they are temporally too close each other. [7] Fig.3 shows the background reduction obtained requiring only one cluster in the ECAL, no hits in vetoes, no γs in the SAC with energy $> 50\,\mathrm{MeV}$ and an energy of the cluster in a range optimized depending on $m_{A'}$.

The DP sensitivity calculation is based on $2.5 \cdot 10^{10}$ GEANT4 simulated 550 MeV positrons on target extrapolated to 10^{13} e^+. This number of particles can be obtained running PADME for 2 y at 60% efficiency with 5000 e^+ per bunch (40 ns) at a repetition rate of 50 Hz. The obtained result for a DP decaying to invisible particles is shown in Fig.4 for different bunch durations: favored $(g-2)_\mu$ region can be explored in a model independent way (the only hypothesis on the DP is the coupling to leptons) up to masses of 23.7 MeV. [7] Single Event Sensitivity (SES) refers to the sensitivity in absence of background.

3 Conclusions

Theoretical models with a DP provide a solution to the DM puzzle. Additionally a DP with mass in the [1 MeV, 1 GeV] interval and coupling constant

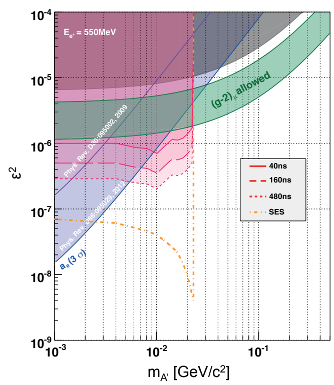

Figure 4: PADME sensitivity to $A' \rightarrow invisible$. Increasing bunch length it is possible to explore smaller ε. SES refers to sensitivity in absence of background.

$\varepsilon \sim 10^{-3}$, can justify the muon anomalous magnetic moment discrepancy.

PADME will perform a model independent search for an invisible decaying DP, using the accelerator complex present at the LNF. The collaboration aims at reaching a sensitivity on ε of $\sim 10^{-3}$ for DP with masses up to 23.7 MeV.

References

1. B. Holdom, Phys. Lett. B **166**, 196 (1986).
2. P. Galison and A. Manohar, Phys. Lett. B **136**,
3. M. Pospelov, Phys. Rev. D **80**, 095002 (2009).
4. B. Echenard, R. Essig and Y. M. Zhong, JHEP **1501**, 113 (2015).
5. R. Essig *et al.*, JHEP **1311**, 167 (2013).
6. M. Raggi and V. Kozhuharov, Riv. Nuovo Cim. **38**, 449 (2015).
7. M. Raggi and V. Kozhuharov, AdHEP **2014**, 959802 (2014).
8. M. Raggi, V. Kozhuharov and P. Valente, EPJ Web Conf. **96**, 01025 (2015).
9. G. Mazzitelli *et al.*, Nucl. Instrum. Meth. A **515**, 524 (2003).

Pulse shape analysis of CUORE-0 bolometers

Daria Santone
Dipartimento di Scienze Fisiche e Chimiche, Università dellAquila, LAquila I-67100 - Italy,
INFN - Laboratori Nazionali del Gran Sasso, Assergi (LAquila) I-67010 - Italy

Abstract

The CUORE experiment search the $0\nu\beta\beta$ of ^{130}Te using the bolometric technique. CUORE-0, a CUORE prototype, has been operating in two last years to test the detector performances. The data collected by CUORE-0 makes it ideal to study the bolometer performances for a future improvement of $0\nu\beta\beta$ sensitivity.

1 Introduction

Neutrinoless double beta decay $0\nu\beta\beta$ is a extremely rare process in which a nucleus undergoes two simultaneous beta decays without neutrino emission. Its evidence is a peak in the sum of energy spectrum of two emitted electrons [1]. This process has never been observed but its discovery would demonstrate the lepton number violation and the Majorana nature of neutrino(ν and $\overline{\nu}$ are the

same particle), it also would constrain the neutrino mass absolute scale [2]. The Cryogenic Underground Observatory for Rare Events (CUORE) [3], which is in the final stage of construction at LNGS, search the $0\nu\beta\beta$ of ^{130}Te. It is an array of 988 TeO_2 crystals arranged in 19 towers for total mass about 750 kg. One CUORE tower consists in 52 crystals disposed in 13 floors, on each floor there are four TeO_2 crystals, each with a mass of 750 g.
CUORE-0, the first CUORE-like tower, has been operating from 2013 to 2015, like CUORE prototype. It demonstrated the efficiency of CUORE assembly line to reduce the α background and that the CUORE crystal energy resolution of 5 keV has been reached [4].
The large amount of data collected by CUORE-0 makes it ideal to study in detail the performance of detector response. The aim of my analysis is the characterization of CUORE-0 bolometer response and behavior for a future improvement of $0\nu\beta\beta$ sensitivity.

2 Bolometric technique and TeO_2 bolometer performance

A bolometer is a low temperature calorimeter in which the energy released into the crystal is converted in a thermal signal. It consists in a dielectric crystal, the absorber, and a thermal sensor, that converts the thermal signal in electrical signal [5].
A CUORE bolometer [6] is a 5x5x5 cm^3 TeO_2 crystal equipped with NTD-Ge (Neutron-Transmutation-Doped germanium) thermal sensor, a germanium crystal doped by thermal neutrons. The CUORE bolometer will operate at 10 mK. At this temperature the thermal capacity of TeO_2 is 2.3 x 10^{-9} J/K. The NTD sensor operates in the Variable Range Hopping regime(VRH): the phonons are responsible of conduction regime and the charge migrate among far impurity sites at Fermi energy. The resistivity is correlated to temperature by the followed relationship:

$$R(T) = R_0 exp \left[\frac{T_0}{T}\right]^{\frac{1}{2}} \tag{1}$$

where R_0 and T_0 depend on the doping concentration, the value for CUORE-NTD are $R_0 \sim 1\Omega$ and $T_0 \sim 4$ K.
The most important parameter is the detector energy resolution because it determinate the power to discriminate the $0\nu\beta\beta$ peak. CUORE-0 estimated the energy resolution exposing each bolometer to a thoriated tungsten source.

The energy resolution has been evaluated on ^{208}Tl photo-peak (2615 keV) because it is the closest high-statistic signal to the ROI (2527.5 keV). The effective mean FWHM value in CUORE-0 is 4.8 keV (Fig.1).

The energy resolution value is not dominated by electronic noise, so the goal

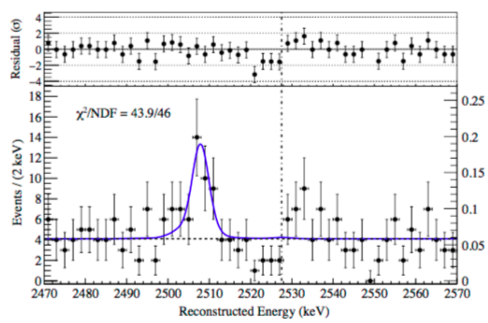

Figure 1: CUORE-0 crystal energy resolution estimated by ^{208}Tl photo-peak

of my analysis is a possible future improvement of energy resolution by a better understanding of bolometer response.

The ideal bolometer response is given by a pulse: the amplitude is proportional to the energy released into the crystal and the decay time is inversely proportional to thermal conductance G. The signal is very slow, so it can be used to search rare events.

Despite this simple model, the actual response is much complex because there are different contribution to the thermal coupling (Fig.2a) [7].

The CUORE crystals are housed in a copper structure by PTFE holders, that also are responsible of the thermal coupling between the absorber and heat bath. The NTD is glued to the crystal by a Araldit rapid epoxy and is connected to the electronic by gold wires, responsible of thermal coupling between sensor and heat bath. The electron/phonon decoupling was also observed in the sensor. The electrons and the phonons are at two different temperatures, so there is a thermal conductance between them. Given this different thermal coupling, the thermal model for a CUORE crystal is described in the figure 2b.

Nevertheless, there is not a full thermal model to describe the bolometer response. Finding the different component of CUORE-0 pulses and correlating them to physics parameters will help in developing a better bolometer thermal

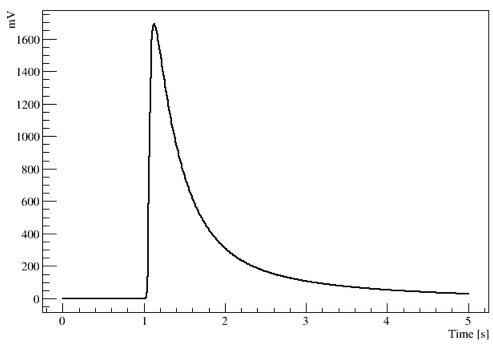

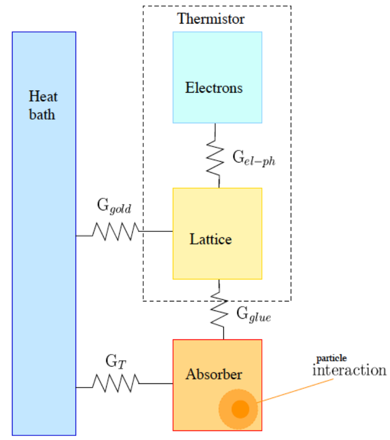

Figure 2: a) An example of CUORE-0 pulse response; b) Thermal model for CUORE-0 bolometers.

model and possible improvement of detector response.

3 Pulse shape analysis

The pulse shape is described by sum of n exponentials and the fit function is given by following form:

$$A_1 exp\left[\frac{(t_0-t)}{t_1}\right]+A_2 exp\left[\frac{(t_0-t)}{t_2}\right]+...-(A_1+A_2+...+A_n)exp\left[\frac{(t_0-t)}{t_r}\right] \quad (2)$$

where t_0 is the trigger time.

The detector response is also influenced by electronic chain effects. They come from the RC filter and 6-poles Bessel filter with a cutoff frequency $\nu_t = 12$ Hz. The RC filter is given by the parasitic capacity c_p of the wiring between the NTD sensor and the electronics. The value of c_p depends on the length of the wires that carry the signal out of cryostat, that is of order of 400 pF. The value of R is the NTD resistance, that is of order 100 MΩ. The 6-poles Bessel filter is used to reduce the aliasing noise in the out-of-band frequency. This filter causes a curvature on the rise of the pulse and a delay of the signal. This effects are simulated by the sigmoid function to simplify the fit computing program.

The fit function is given by:

$$\frac{1}{1+exp[-sigma(t-s_0)]}\times CONV[\left(\frac{1}{RC}exp\left[-\frac{t}{RC}\right]\right), pulseshape(A_i, t_r, t_{d_i})] \tag{3}$$

where the sigmoid parameters are the curvature on the rise ($sigma$) and the delay of the pulse (s_0).
The first step is to define how many time constants describe the pulse shape. The figure 3 shows two examples fit of 2615 keV γ-ray pulse. The one on the left is a sum of four exponentials (one rise plus three decays) and the one on the right is a sum of five exponentials (one rise plus four decays).
The fit residuals show that the five exponentials fit describe much better the pulse shape, especially in the first part of the pulse (fig.4).

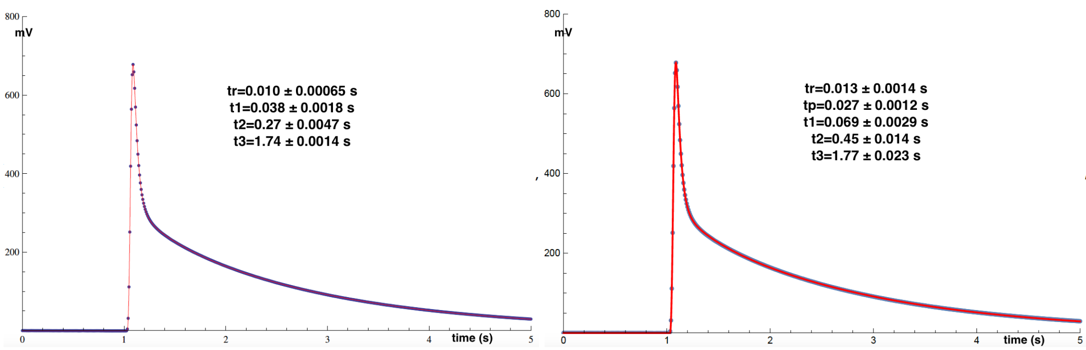

Figure 3: a) Four exponentials fit b) Five exponentials fit

It also observed that the first time decay t_p is correlated to a platinum contamination present in the TeO_2 crystals. This contamination originatas during TeO_2 crystals growth, because the crucibles are made of platinum foil. The platinum contamination is estimated looking at the ^{190}Pt peak counting rate in the energy range 3200 - 3400 keV for each crystal [8].
The time constant t_p shows up only for ^{190}Pt rate upper than 150 count/kg/years. At lower rate t_p is not necessary to describe the pulse shape, although the response is influenced by platinum heat capacity. In fact the estimation of t_r, t_1 and t_2 is correlated to platinum rate (Fig.5).

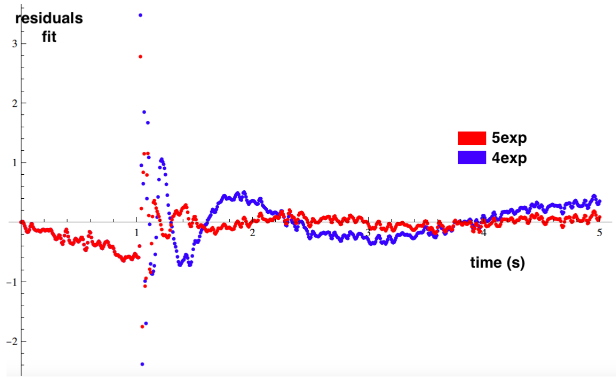

Figure 4: Comparison between four and five exponential fit residuals

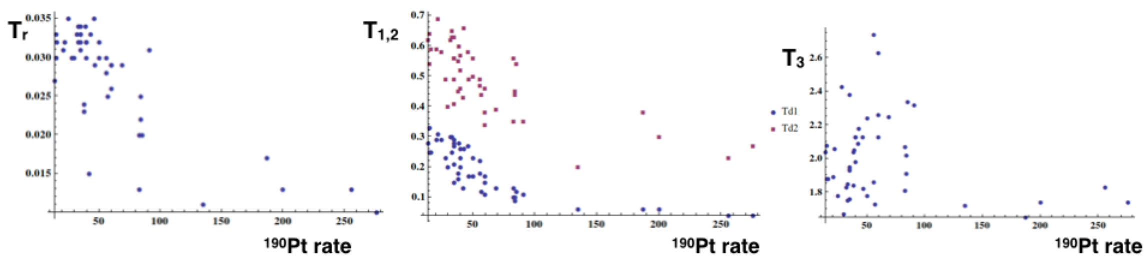

Figure 5: Time constant estimation vs Platinum rate.

References

1. J. D Vergados, H. Ejiri, F. Simkovic, Rep. Prog. Phys. 75 (2012).
2. A. Strumia, F. Vissani, arXiv.org/abs/hep-ph/0606054 (2010)
3. C. Arnaldoldi *et al.*, Nucl.Instr.Meth. (2004)
4. CUORE Collaboration, Phys.Rev.Lett.115 no.10, 102502 (2015)
5. K. Petzl, Nucler Instruments and Metods in Physic Reserch (2000)
6. CUORE Collaboration, arXiv:1604.05465 (2016)
7. M. Carattoni, M. Vignati, Journal of Instrumentation, Vol.6 (2011)
8. F. Alessandria *et.al.*, Astropart.Phys.35, 893-849 (2012)

The Fermilab Muon g-2 experiment

Nandita Raha, on behalf of the Muon g-2 Collaboration
INFN, Sezione di Roma Tor Vergata, Roma, Italy,

Abstract

The anomalous magnetic moment of the muon can be both measured and computed to a very high precision, making it a powerful probe to test the standard model and search for new physics. The previous measurement by the Brookhaven E821 experiment found about three standard deviation discrepancy from the predicted value. The Muon g-2 experiment at Fermilab will improve the precision by a factor of four through a factor of twenty increase in statistics and a threefold reduced systematic uncertainty with an upgraded apparatus. The experiment will also carry out an improved measurement of the muon electric dipole moment. Construction at Fermilab is well underway.

1 Introduction and theoretical background

The muons magnetic moment $\vec{\mu}$ is given by,

$$\vec{\mu} = g\frac{q}{2m}\vec{s} \tag{1}$$

where the gyromagnetic ratio g of the muon is predicted to be 2 in case of structureless spin 1/2 particle of mass m and charge q, according to Dirac theory. Experimentally it is measured to be greater than 2. The muon anomaly a_μ, given by (g-2)/2 arises due to radiative corrections (RC), which couple the muon spin to virtual fields. These mainly include quantum electrodynamic processes (QED), electroweak loops, hadronic vacuum polarization (HVP) etc. as shown in Fig.1.

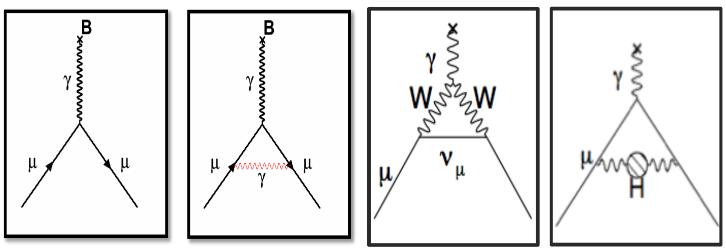

Figure 1: The SM correction in a_μ from QED, electroweak loops, HVP.

The leading RC from the lowest order QED process from the exchange of a virtual photon in Fig.1 i.e. the “Schwinger term”, is calculated to be $a_\mu = (\alpha/2\pi) = 0.00116$ [1]. The difference between experimental and theoretical values of a_μ especially at sub-ppm precision, explores new physics well above the 100 GeV scale for many standard model extensions [2].

A difference of 3.6 σ [3] between theory and experiment, could indicate several possible models or any new model. These new models, can be generally illustrated using a relation discussed in [4] in which new physics (N.P.) contributions scale as [5] $\delta a_\mu(N.P.) = \mathcal{O}[C(N.P.)] \times (m_\mu/M)^2$ where M is the N.P. mass scale and C is the model's coupling strength, related to any N.P. contributions to the muon mass, $C(N.P.) \equiv (\delta m_\mu(N.P.)/\delta m_\mu)$. In the multi-TeV scale, a muon mass is generated by radiative effects (shown in green in Fig.2). The other possible models could be due to Z′, W′, universal extra dimensions, littlest Higgs assume a typical weak-interaction scale coupling (shown in red in Fig.2) [5]. The purple band in this figure represents unparticles, extra dimension models or SUSY with enhanced coupling [6]. Existence of dark photons or dark Z [7] from very weakly interacting and very light particles would correspond to a narrow band in the 10 - 100 MeV mass range, having an extremely small coupling, is not shown in this figure. In Fig.2 the yellow band represents the difference between theory and experiment and the blue band represents the improvement with combined theory and experimental error. Improved precision of measurement in a_μ to 140 parts per billion will continue to constrain or validate the energy scale of the models, which is the goal of "The E989 Muon g-2 Experiment". This requires 21 times more statistics than the previous Brookhaven E821 experiment and a threefold reduction of the systematic error.

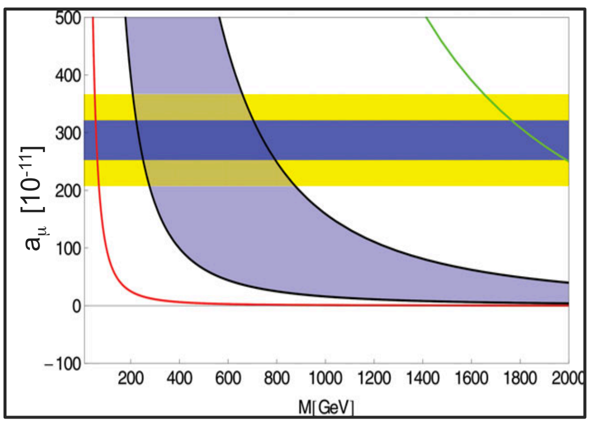

Figure 2: Generic classification of mass scales vs. a_μ contributions from new physics sources. Various possibilities are explained in Sec.1.

2 Storage ring technique

A polarized muon beam (from pion decay) of energy of 3.1 GeV is injected (through the inflector shown in Fig.3) in a storage ring of uniform magnetic field of 1.45 T with a cyclotron frequency of ω_c. Fig.3 shows the entire storage ring with the kickers (K1-K3), and the quadrupoles (Q1-Q4), the collimators (C), the NMR trolley garage and the fiber harps. An electron calorimeter is placed at a position indicated by the calorimeter number (1 to 24). We essentially measure the muon spin precession frequency ω_s relative to the cyclotron frequency i.e. $\omega_a = \omega_s - \omega_c$.

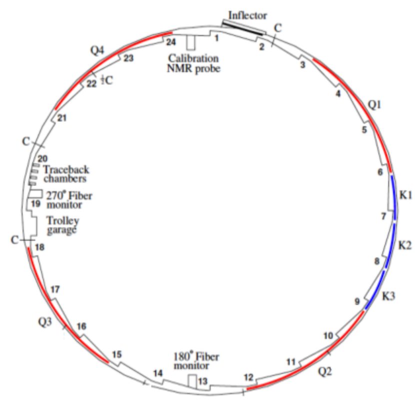

Figure 3: The layout of the storage ring from the E821 experiment.

These frequencies including Larmor and Thomas precession are approximately given by,

$$\begin{aligned} \omega_c &= \frac{e}{m\gamma}B \\ \omega_S &= \frac{e}{m\gamma}B(1+\gamma a_\mu) \\ \omega_a &= \frac{eB}{m}a_\mu \end{aligned} \tag{2}$$

Thus, a_μ is extracted from ω_a, provided the magnetic field B is measured via NMR and recast a_μ in terms of proton precession frequency ω_p,

$$a_\mu = \frac{\omega_a/\omega_p}{\mu_\mu/\mu_p - \omega_a/\omega_p} \tag{3}$$

The measurement of a_μ also requires an accurate value of μ_μ/μ_p as seen in Eq.3. The muons decay to positrons preferentially in direction of muon spin which are detected by the 24 calorimeters shown in Fig.3. The time spectrum of these positrons is given by,

$$N(t) = N_0 e^{-t/\tau}(1 + Acos(\omega_a t)) \tag{4}$$

with which ω_a is extracted. But care needs to be taken into account for the distortions in this spectrum due to pileup, gain instabilities, beam losses.

3 Experimental progress and details

The storage ring layout is shown in Fig.3 of the previous section. Here we emphasize on the details of the improvements required to achieve our goal. Several improvements are required to collect 21 times more muons than the previous effort at Brookhaven E821 experiment. This is accomplished by improved muon storage and using a long decay channel to produce muons that requires improvement of existing tunnels and building new ones. The usage of a delivery ring to get rid of pions would eliminate early unwanted background. The improved beam structure will have 4 batches of 4×10^{12} protons to the Recycler in 1.33 s supercycle with a frequency of 15 Hz. A proton batch is divided into four proton bunches of intensity 10^{12}. Thus, the experiment will receive 16 proton bunches per supercycle, i.e. a rate of 12 Hz.

We aim for enhanced improvements to the muon precession systematics due to calorimeters and trackers. To achieve this the calorimeter should resolve multiple particles and have high gain stability. Each calorimeter is made up of 9×6 PbF_2 Cherenkov crystals that are read by SiPMs (Silicon Photo Multipliers) which improves the resolution and pileup protection. A laser calibration system will be used for the accurate calibration of the calorimeters. We will develop a high-performance laser calibration system and use it for on-line monitoring of the SiPM gain fluctuations during the run. This laser calibration system must have a relative accuracy at sub-per mil level to achieve the goal of our experiment. The tracker should improve positron tracking (use much thinner straws) and inform muon beam dynamics more effectively.

We further aim for improvements to the proton precession systematics by using new set of NMR probes and generating a more uniform magnetic field with improved shimming of magnets. A uniform field is essential as the signal degrades more quickly in high gradients. The magnetic field is measured using pulsed proton NMR with a goal of 70 ppb accuracy. The factor of 2.4 improvement over BNL E821 will come from higher magnetic field uniformity and stability, new lower noise NMR electronics with higher frequency resolution, new NMR probes with higher signal to noise ratio and improved calibration probes and calibration techniques.

4 Summary

The Muon g-2 experiment under construction at Fermilab aims for a fourfold improvement from Brookhaven E821 in the measurement of the muon g-2. This is essential for the understanding of QED and the Standard Model and evidence of any new physics beyond the Standard Model. Significant efforts in the theory of e^+e^- measurements are also leading to an improvement in the uncertainty in HVP along with a lot of progress on Lattice calculations too. This will improve the theoretical calculation of g-2. Efforts to enhance and investigate the performance of all detector systems are taking place, along with testing the best methods of data acquisition. We plan further installations in 2^{nd} half of 2016 and expect data taking with muons in 2017 and initial results in 2018.

Acknowledgments

This work was supported by the EU Horizon 2020 Research and Innovation Programme under the Marie Sklodowska-Curie Grant Agreement No. 690835.

References

1. J. Schwinger, Phys. Rev. 73, 416 (1948).
2. G.W. Bennett, et al. Phys.Rev.D73:072003, 2006
3. Davier et al. 2011
4. A. Czarnecki and W. J. Marciano, Phys. Rev. D64, 013014 (2001)
5. D. Hertzog, Ann. Phys (Berlin) 2015., courtesy D. Stockinger
6. T. P. Gorringe and D. W. Hertzog, doi: 10.1016/j.ppnp.2015.06.001
7. H. Davoudiasl, et al. Phys. Rev. D **86** (2012) 095009

Design, R&D and status of the crystal calorimeter for the Mu2e experiment

Raffaella Donghia on behalf of the Mu2e calorimeter group
Universitá degli Studi Roma Tre, Rome, Italy,
Laboratori Nazionali di Frascati - INFN, Frascati, Italy

Abstract

The Mu2e Experiment at Fermilab will search for coherent, neutrinoless conversion of muons into electrons in the field of a nucleus, with a sensitivity improvement of a factor of 10^4 over previous experiments. Such a charged lepton flavor-violating reaction probes new physics at a scale inaccessible with direct searches at either present or planned high energy colliders.

The conversion electron is mono-energetic with an energy slightly below the muon rest mass. If no events are observed in three years of running, Mu2e will set a limit on the ratio between the conversion rate and the capture rate, $R_{\mu e}$, of $\leq 6 \times 10^{-17}$ (@ 90% CL).

In this paper, the physics motivation for Mu2e and the current status of the electromagnetic calorimeter project are briefly presented.

1 Introduction

The Mu2e experiment at Fermilab [1] will search for the charged lepton flavor violating (CLFV) process of muon conversion in an ^{27}Al nucleus field, $\mu + N(Z,A) \rightarrow e + N(Z,A)$. No CLFV interactions have been observed experimentally yet. The current best limit on $\mu - e$ conversion has been set by SINDRUM II experiment. [2] Mu2e intends to probe 4 orders of magnitude beyond the SINDRUM II sensitivity, measuring the ratio, $R_{\mu e}$, between the conversion rate to number of muon captures by Al nucleus:

$$R_{\mu e} = \frac{\mu^- \, N(Z,A) \rightarrow e^- \, N(Z,A)}{\mu^- \, N(Z,A) \rightarrow \nu_\mu \, N(Z-1,A)} < 6 \times 10^{-17}, \text{ (@ } 90\% CL)$$

The signature of this neutrinoless conversion process is a monoenergetic electron, with an energy slightly lower than the muon rest mass, ~ 104.96 MeV. In order to achieve our goal, a very intense muon beam ($\sim 10^{10}$ Hz) has to stop on an aluminum target and a precise momentum analysis has to be performed.

In the Standard Model (SM) the expected rate is negligible (BR $\sim 10^{-54}$), so that, observation of these processes should be crucial evidence of New Physics beyond the SM. [3]

2 Calorimeter requirements

The Mu2e calorimeter is designed to identify ~ 100 MeV electrons and to reduce the background to a negligible level. It is located inside a large superconducting solenoid, just behind the tracker, which complements it. Indeed, the calorimeter provides information about energy, timing and position to validate charged particles reconstructed by the tracker and reject fakes. Moreover, the calorimeter has to perform a particle identification to distinguish muons from electrons. These tasks lead to the following requirements [1]: an energy resolution around 5% (5 MeV, at 100 MeV); a timing resolution better than 0.5 ns; a position resolution better than 1 cm; little deterioration for radiation exposures up to ~ 100 krad in the hottest region and for a neutron flux equivalent to 10^{12} MeV/cm^2;Moreover, the Mu2e calorimeter must operate in 10^{-4} Torr internal pressure within the 1 T magnetic field. This implies the use of solid-state photodetectors and of electronics (HV and FEE) immune to the presence of the magnetic field.

3 Calorimeter design

In the 100 MeV energy regime, a total absorption calorimeter employing a homogeneous continuous medium is required to meet the Mu2e requirements.

We decided to adopt a solution with two annular disks made by scintillating crystals, each readout using two solid state photon-counters. Each disk (Fig. 1, left) has an internal (external) radius of 374 mm (660 mm) and is filled with 674 $(34 \times 34 \times 200)$ mm^3 crystals. The two disks are separated by about half electron wavelength (70 cm).

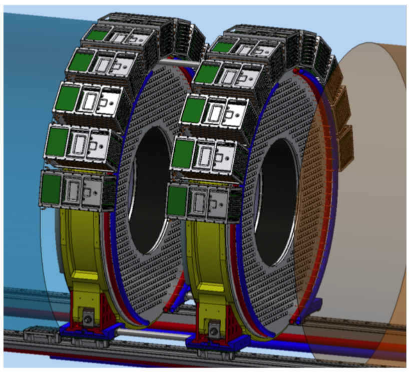

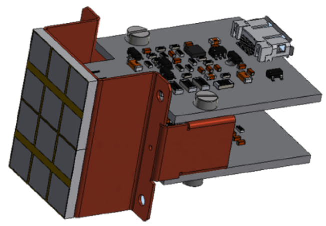

Figure 1: Annular disks structure of the Mu2e electromagnetic calorimeter (left). Layout of the 2 SiPMs coupled to each crystal, with the analog read out electronics connected.

Due to the physical and geometrical constraints stated, crystals with high light output (LY), good light response uniformity (LRU $\geq$ 10%), fast signal ($\tau \leq 40$ ns), radiation hard (with maximum LY loss below 40%) and small radiation induced readout noise (below 0.6%) are needed.

Different types of crystals have been considered: lutetium-yttrium oxy-orthosilicate (LYSO), Barium Fluoride (BaF_2) and pure Cesium Iodide (CsI). In the CDR [4], the baseline calorimeter choice was LYSO crystals readout with APD and many tests were carried out for this option. [5] A large increase price in 2013 made this option unaffordable, so that for the TDR [1] we have opted for cheaper crystals such as BaF_2 and CsI. After a long R&D program, we have finally selected undoped CsI crystals as baseline choice. [6] [7]

The CsI crystals readout is done by UV-extended silicon photomultipliers (SiPMs). The requirement of having a small air gap between crystal and photodetector and the request of redundancy in the readout implies the use of custom devices. For the Mu2e experiment we have increased the transversal dimension of the CsI from (30×30) to (34×34) mm^2 in order to accomodate two (2×3) arrays of 6×6 mm^2 UV-extended SiPM. The samples already procured show a good PDE ($\sim$ 30% at 315 nm) with a gain greater than 10^6 at the operation voltage.

Each SiPM is directly connected to the readout electronics (Fig. 1, right) and to a dedicated board housing a transimpedence preamplifier with a settable gain ×15 or ×30, 2 V dynamic range and 15 ns rise time. This digital boards are housed into 11 crates (in the top of each disk) per disk with 20 differential channels per board. These boards are composed by a mezzanine board for input of SIPM signals and HV setting and a Waveform Digitizer section based on SmartFusione II FPGA with 200 Msps 12 bit ADC.

4 Characterization of calorimeter parameters

Tests on CsI crystals have been performed with ^{22}Na source for three different vendors: ISMA (Ukraine), SICCAS (China) and Opto Materials (Italy). All tested crystals show a good LY ~ 120 photoelectrons per MeV and a $\sim 0.6\%$/cm LRU when coupled with an UV-extended photomultiplier (PMT) and Tyvek wrapping (Fig. 2, left). Exploiting cosmic rays and using a single (2×3) array

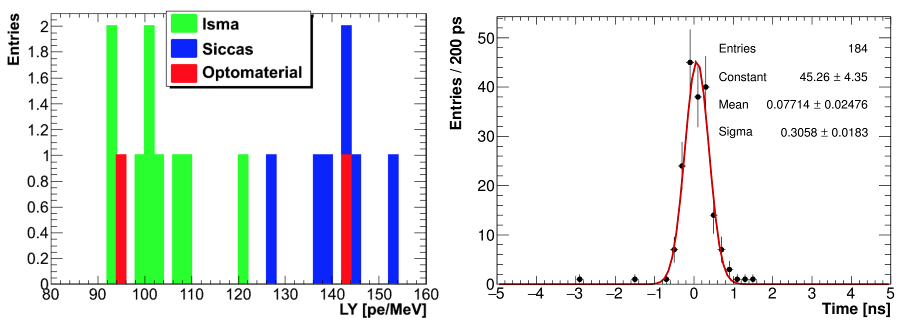

Figure 2: Average LY of all the crystals tested (left) and time resolution of an Opto Materials crystal coupled with a single (2×3) array of 6×6 mm^2 Hamamatsu SiPM (right).

of 6×6 mm^2 Hamamatsu [8] SiPM as readout , we have evaluated also the time resolution, which is ∼170 ps (@ ~ 22 MeV, energy deposited by a minimum ionizing particle in a CsI crystal) after subtracting the 255 ps of the trigger time resolution (Fig. 2, right).

Following calorimeter requirements, one important aspect to be considered is the radiation hardness. In this context, we have performed different tests both on crystals and SiPMs from different vendors.

Some crystals have been irradiated up to 900 Gy and to a neutron fluency up to 9×10^{11} n_{1MeV}/cm^2. The ionization dose does not modify LRU while a 20% reduction in LY has been observed at 900 Gy. Similarly, the neutron flux causes a 15% LY deterioration. Moreover, it is important to control the noise induced by the instantaneous dose (2 rad/h) and thermal neutron flux (10 kHz/cm^2). For this purpose, a crystal readout by a PMT has been irradiated in these conditions and the photocurrent has been recorded. The energy equivalent noise, RIN, was derived as the standard deviation of the number of photoelectron, N, in a readout gate of 200 ns:

$$RIN = \frac{\sqrt{N}}{LY}(MeV) \tag{1}$$

We have measured the RIN from dose and thermal neutrons for crystals from the three vendors. Our results show the RIN from γ-ray in the hottest region to be around 300 keV. For thermal neutrons the RIN is much lower: 60-85 keV for a flux of 10^4 n/cm^2/s.

UV-extended SiPM, both Hamamatsu and FBK [9] companies, have been irradiated with a dose up to 20 krad, which did not effect the leakage current. On the contrary, a current increase is clearly visible in all SiPMs when exposing the sensors to a total flux of 2.2×10^{11} n/cm^2 (corresponding to 2.2 times the experiment lifetime) [7]: the leakage current of the Hamamatsu SiPM increased from ~ 16 μA to ~ 2 mA while the FBK one from $\sim$ 21 μA to $\sim$ 5 mA. Even if the hall temperature was quite stable during irradiation the drop on the gain was mostly dominated by the temperature increase of the SiPMs. To reduce it to acceptable value, we need to cool down all SiPM to a temperature of 0°C. In order to do so, we will use a dedicated cooling station for the calorimeter, which is now under design.

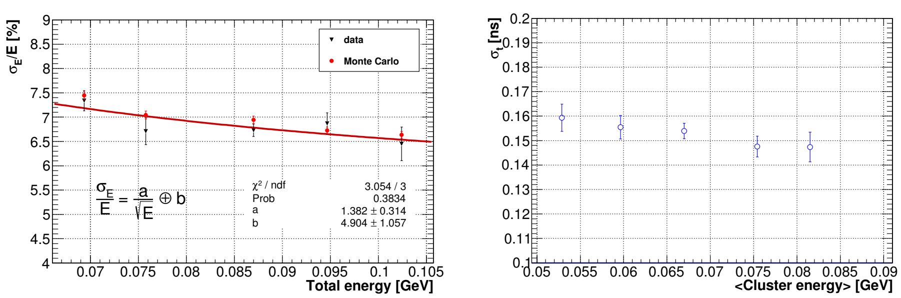

Figure 3: Energy (left) and time (right) resolution at different electron beam energies of the 3×3 CsI matrix.

Finally, a small undoped CsI 3×3 matrix has been built and tested at the Frascati Beam Test Facility using electrons with energy between 80 and 120

MeV. Each crystal is read out using an array of sixteen (3×3) mm^2 Hamamatsu TSV SiPMs. During this test we measured a LY of 30 (20) pe/MeV with (without) optical grease with Tyvek wrapping. The measured time and energy resolution are 110 ps and 7% respectively (Fig. 3).

These performance results, both of single crystals and of the small calorimeter prototype, are fully compatible with the requirements of the calorimeter. We are now preparing the international bid for the procurement of the pre-production and production crystals and sensors.

Acknowledgments

Talk given at the 5th Young Researchers Workshop "Physics Challenges in the LHC Era", Frascati, May 9 and 12, 2016

This work was supported by the EU Horizon 2020 Research and Innovation Programme under the Marie Sklodowska-Curie Grant Agreement No. 690835.

References

1. L. Bartoszek et al., (Mu2e experiment), "Mu2e Technical Design Report" arXiv:1501.05241 (2015).
2. H. Wilhelm et al. (SINDRUM II Collaboration), "A Search for muon to electron conversion in muonic gold", Eur. Phys. J. C47 337-346 (2006).
3. A. de Gouvea and P. Vogel, "Lepton Flavor and Number Conservation, and Physics Beyond the Standard Model", Progress in Particle and Nuclear Physics, Vol 71, pag. 75-92, arXiv:1303.4097 (2013).
4. J. Abrams et al., "Mu2e conceptual design report" arXiv:1211.7019 (2012).
5. N. Atanov et al., "Measurement of time resolution of the Mu2e LYSO calorimeter prototype", Nucl. Instrum. Meth. A812 104 doi:10.1016/j.nima.2015.12.055, arXiv:1509.04468 (2016).
6. N. Atanov et al., "Longitudinal uniformity, time performances and irradiation test of pure CsI crystals", Nucl. Inst. Meth. in Phys. Research, A, pp. 678-680 doi:10.1016/j.nima.2015.11.042 (2016).
7. S. Baccaro et al., "Radiation hardness test of un-doped CsI crystals and Silicon Photomultipliers for the Mu2e calorimeter" arXiv (2016).
8. http://www.hamamatsu.com/us/en/index.html
9. https://srs.fbk.eu

BFKL phenomenology: resummation of high-energy logs in semi-hard processes at LHC

Francesco Giovanni Celiberto
Dipartimento di Fisica, Università della Calabria,
Istituto Nazionale di Fisica Nucleare, Gruppo Collegato di Cosenza
Arcavacata di Rende, 87036 Cosenza, Italy

Abstract

A study of differential cross sections and azimuthal observables for semi-hard processes at LHC energies, including BFKL resummation effects, is presented. Particular attention has been paid to the behaviour of the azimuthal correlation momenta, when a couple of forward/backward jets or identified hadrons is produced in the final state with a large rapidity separation. Three- and four-jet production has been also considered, the main focus lying on the definition of new, generalized azimuthal observables, whose dependence on the transverse momenta and the rapidities of the central jet(s) can be considered as a distinct signal of the onset of BFKL dynamics.

1 Introduction

The large amount of data already recorded and to be produced in the near future at the Large Hadron Collider (LHC) offers a peerless opportunity to probe perturbative QCD at high energies. Multi-Regge kinematics (MRK), which prescribes the production of strongly rapidity-ordered objects in the final state, is the key point for the study of semi-hard processes in the high-energy limit. In this kinematical regime, the Balitsky-Fadin-Kuraev-Lipatov (BFKL) approach, at leading (LL) [1–6] and next-to-leading (NLL) [7, 8] accuracy, represents perhaps the most powerful tool to perform the resummation of large logarithms in the colliding energy to all orders of the perturbative expansion. So far, Mueller–Navelet jet production [9] has been the most studied reaction. Interesting observables associated to this process are the azimuthal correlation momenta, which, however, are strongly affected by collinear contaminations. Therefore, new observables, independent from these contaminations, were proposed in [10, 11] and calculated at NLL in [12–21], showing a very good agreement with experimental data at the LHC. Unfortunately, Mueller–Navelet configurations are still too inclusive to perform MRK precision studies. With the aim to further and deeply probe the BFKL dynamics, we propose to investigate two different kinds of processes. The first one is the detection of two charged light hadrons: $\pi^{\pm}$, $K^{\pm}$, p, $\bar{p}$ having high transverse momenta and separated by a large interval of rapidity, together with an undetected hadronic system X [22, 23]. On one side, hadrons can be detected at the LHC at much smaller values of the transverse momentum than jets, allowing us to explore a kinematic range outside the reach of the Mueller–Navelet channel. On the other side, this process makes it possible to constrain not only the parton densities (PDFs) for the initial proton, but also the parton fragmentation functions (FFs) describing the detected hadron in the final state. The second kind of processes is the multi-jet production [24–27], which allows to define new, generalized and suitable BFKL observables by considering extra jets well separated in rapidity in the final state and by studying the dependence on their transverse momenta and azimuthal angles.

2 Di-hadron production

We consider the production, in high-energy proton-proton collisions, of a pair of identified hadrons with large transverse momenta, $\vec{k}_1^2 \sim \vec{k}_2^2 \gg \Lambda^2_{\rm QCD}$ and large separation in rapidity. The differential cross section of the process reads

$$\frac{d\sigma^{\rm di-hadron}}{dy_1 dy_2\, d|\vec{k}_1|\, d|\vec{k}_2| d\phi_1 d\phi_2} = \frac{1}{(2\pi)^2}\left[\mathcal{C}_0 + \sum_{n=1}^{\infty} 2\cos(n\phi)\mathcal{C}_n\right] , \tag{1}$$

where $\phi = \phi_1 - \phi_2 - \pi$, with $\phi_{1,2}$ the two hadrons' azimuthal angles, while $y_{1,2}$ and $\vec{k}_{1,2}$ are their rapidities and transverse momenta, respectively. In order to match the kinematic cuts used by the CMS collaboration, we consider the *integrated azimuthal coefficients* given by

$$C_n = \int_{y_{1,\min}}^{y_{1,\max}} dy_1 \int_{y_{2,\min}}^{y_{2,\max}} dy_2 \int_{k_{1,\min}}^{\infty} dk_1 \int_{k_{2,\min}}^{\infty} dk_2 \delta\left(y_1 - y_2 - Y\right) \mathcal{C}_n \tag{2}$$

and their ratios $R_{nm} \equiv C_n/C_m$. For the integrations over rapidities and transverse momenta we use the limits, $y_{1,\min} = -y_{2,\max} = -2.4$, $y_{1,\max} = -y_{2,\min} = 2.4$, $k_{1,\min} = k_{2,\min} = 5$ GeV, which are realistic values for the identified hadron detection at LHC. In Fig. 1 the dependence on the rapidity separation between the detected hadrons, $Y = y_1 - y_2$, of the ϕ-averaged cross section C_0 and of the ratios R_{10} and R_{20} at the center-of-mass energy $\sqrt{s} = 13$ TeV is shown.

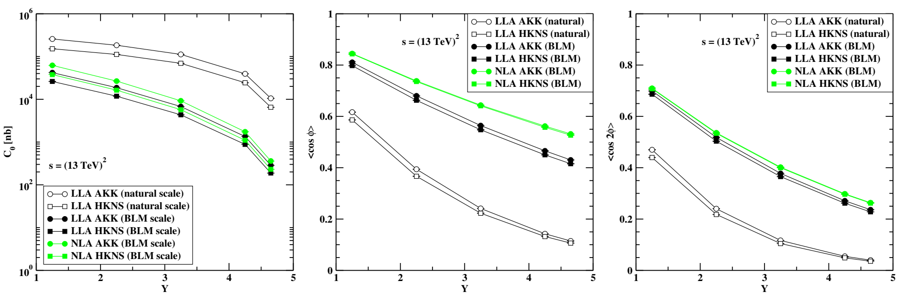

Figure 1: Y dependence of cross section, $\langle \cos\phi \rangle$ and $\langle \cos 2\phi \rangle$ for di-hadron production at $\sqrt{s} = 13$ TeV. See Ref. [23] for the FF parametrizazions used and for the definition of "natural" and "BLM" scales.

3 Multi-jet production

The process under investigation is the hadroproduction of n jets in the final state, well separated in rapidity so that $y_i > y_{i+1}$ according to MRK, and with their transverse momenta $\{k_i\}$ lying above the experimental resolution scale, together with an undetected soft-gluon radiaton emission. Pursuing the goal to generalize the azimuthal ratios R_{nm} defined for Mueller–Navelet jet and di-hadron production, we define new, generalized azimuthal correlation momenta by projecting the differential cross section $d\sigma^{n-\text{jet}}$ on all angles, so having

$$\mathcal{C}_{M_1 \cdots M_{n-1}} = \left\langle \prod_{i=1}^{n-1} \cos\left(M_i \, \phi_{i,i+1}\right) \right\rangle = \int_0^{2\pi} d\theta_1 \cdots \int_0^{2\pi} d\theta_n \prod_{i=1}^{n-1} \cos\left(M_i \, \phi_{i,i+1}\right) d\sigma^{n-\text{jet}} \tag{3}$$

where $\phi_{i,i+1} = \theta_i - \theta_{i+1} - \pi$, with θ_i being the azimuthal angle of the jet i. Firstly, we introduce realistic LHC kinematical cuts by integrating $\mathcal{C}_{M_1 \cdots M_{n-1}}$

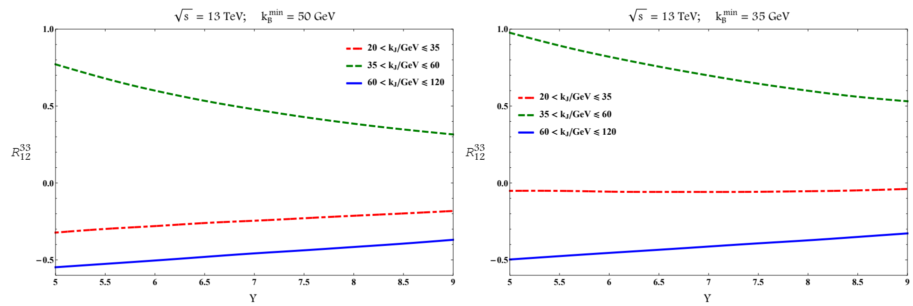

Figure 2: Y dependence of R_{12}^{33} for $\sqrt{s} = 13$ TeV and $k_{B,\min} = 50$ GeV (left column) and $k_{B,\min} = 35$ GeV (right column). $k_{A,\min}$ is fixed to 35 GeV, while the central jet has rapidity $y_J = (y_A + y_B)/2$.

over rapidities and momenta of the tagged jets

$$C_{M_1 \cdots M_{n-1}} = \int_{y_{1,\min}}^{y_{1,\max}} dy_1 \cdots \int_{y_{n,\min}}^{y_{n,\max}} dy_n \int_{k_{1,\min}}^{\infty} dk_1 \cdots \int_{k_{n,\min}}^{\infty} dk_n \delta\left(y_1 - y_n - Y\right) \mathcal{C}_n \tag{4}$$

and by keeping fixed the rapidity difference $Y = y_1 - y_n$ between the most forward and the most backward jet, which corresponds to the maximum rapidity interval in the final state. Secondly, we remove the zeroth conformal spin contribution responsible for any collinear contamination and we minimise possible higher-order effects by studying the ratios $R_{N_1 \cdots N_{n-1}}^{M_1 \cdots M_{n-1}} \equiv C_{M_1 \cdots M_{n-1}} / C_{N_1 \cdots N_{n-1}}$ where $\{M_i\}$ and $\{N_i\}$ are positive integers. In Fig. 2 we show the dependence on Y of the coefficient R_{12}^{33}, characteristic of the 3-jet production process, for $\sqrt{s} = 13$ TeV, for two different kinematical cuts on the transverse momenta $k_{A,B}$ of the external jets and for three different ranges of the central jet transverse momentum k_J. In Fig. 3 we show the dependence on Y of the coefficient R_{112}^{221}, characteristic of the 4-jet production process, for $\sqrt{s} = 7$ and 13 TeV, for asymmetrical cuts on the transverse momenta $k_{A,B}$ of the external jets and for two different configurations of the central jet transverse momenta $k_{1,2}$. A comparison with predictions for these observables from fixed order analyses as well as from the BFKL inspired Monte Carlo `BFKLex` [28–32] is underway.

4 Conclusions

We perfomed a study of perturbative QCD in the high-energy limit through two different classes of processes. First we investigated the behaviour of cross section and azimuthal ratios for di-hadron production, which represents a less inclusive final state process with respect to the well known Mueller–Navelet jet

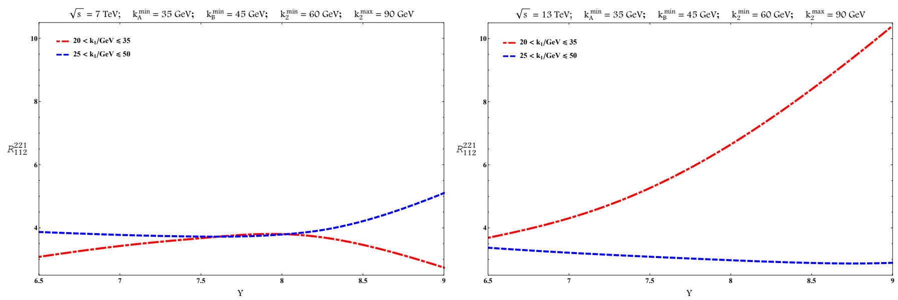

Figure 3: Y dependence of R_{112}^{221} for $\sqrt{s} = 7$ TeV (left column) and for $\sqrt{s} = 13$ TeV (right column). The rapidity interval between a jet and the closest one is fixed to $Y/3$.

reaction. Then we proposed to study multi-jet production processes, in order to define new, generalized and suitable BFKL observables. The comparison with experimental data will help to gauge and disentangle the applicability region of the BFKL formalism, therefore it is needed and suggested.

References

1. L.N. Lipatov, Sov. Phys. JETP **63** (1986) 904 [Zh. Eksp. Teor. Fiz. **90** (1986) 1536].
2. I.I. Balitsky and L.N. Lipatov, Sov. J. Nucl. Phys. **28** (1978) 822 [Yad. Fiz. **28** (1978) 1597].
3. E.A. Kuraev, L.N. Lipatov and V.S. Fadin, Sov. Phys. JETP **45** (1977) 199 [Zh. Eksp. Teor. Fiz. **72** (1977) 377].
4. E.A. Kuraev, L.N. Lipatov and V.S. Fadin, Sov. Phys. JETP **44** (1976) 443 [Zh. Eksp. Teor. Fiz. **71** (1976) 840] [Erratum-ibid. **45** (1977) 199].
5. L.N. Lipatov, Sov. J. Nucl. Phys. **23** (1976) 338 [Yad. Fiz. **23** (1976) 642].
6. V.S. Fadin, E.A. Kuraev and L.N. Lipatov, Phys. Lett. B **60** (1975) 50.
7. V.S. Fadin and L.N. Lipatov, Phys. Lett. B **429** (1998) 127 [hep-ph/9802290].
8. M. Ciafaloni and G. Camici, Phys. Lett. B **430** (1998) 349 [hep-ph/9803389].
9. A.H. Mueller and H. Navelet, Nucl. Phys. B **282** (1987) 727.
10. A. Sabio Vera, Nucl. Phys. B **746** (2006) 1 [hep-ph/0602250].
11. A. Sabio Vera and F. Schwennsen, Nucl. Phys. B **776** (2007) 170 [hep-ph/0702158 [HEP-PH]].

12. D. Colferai, F. Schwennsen, L. Szymanowski, S. Wallon, JHEP **1012** (2010) 026 [arXiv:1002.1365 [hep-ph]].
13. B. Ducloué, L. Szymanowski, S. Wallon, JHEP **1305** (2013) 096 [arXiv:1302.7012 [hep-ph].
14. B. Ducloué, L. Szymanowski, S. Wallon, Phys. Rev. Lett. **112** (2014) 082003 [arXiv:1309.3229 [hep-ph]].
15. B. Ducloué, L. Szymanowski, S. Wallon, Phys. Lett. B **738** (2014) 311 [arXiv:1407.6593 [hep-ph]].
16. F. Caporale, D.Yu. Ivanov, B. Murdaca and A. Papa, Eur. Phys. J. C **74** (2014) 3084 [arXiv:1407.8431 [hep-ph]].
17. F.G. Celiberto, D.Yu. Ivanov, B. Murdaca and A. Papa, Eur. Phys. J. C **75** (2015) no.6, 292 [arXiv:1504.08233 [hep-ph]].
18. F.G. Celiberto, D.Yu. Ivanov, B. Murdaca and A. Papa, Eur. Phys. J. C **76** (2016) no.4, 224 [arXiv:1601.07847 [hep-ph]].
19. R. Ciesielski, arXiv:1409.5473 [hep-ex].
20. M. Angioni, G. Chachamis, J.D. Madrigal and A. Sabio Vera, Phys. Rev. Lett. **107**, 191601 (2011) [arXiv:1106.6172 [hep-th]].
21. G. Chachamis, arXiv:1512.04430 [hep-ph].
22. D.Yu. Ivanov and A. Papa, JHEP **1207** (2012) 045 [arXiv:1205.6068 [hep-ph]].
23. F.G. Celiberto, D.Yu. Ivanov, B. Murdaca and A. Papa, arXiv:1604.08013 [hep-ph].
24. F. Caporale, G. Chachamis, B. Murdaca and A. Sabio Vera, Phys. Rev. Lett. **116** (2016) no.1, 012001 [arXiv:1508.07711 [hep-ph]].
25. F. Caporale, F.G. Celiberto, G. Chachamis and A. Sabio Vera, Eur. Phys. J. C **76** (2016) no.3, 165 [arXiv:1512.03364 [hep-ph]].
26. F. Caporale, F.G. Celiberto, G. Chachamis, D.G. Gómez and A. Sabio Vera, arXiv:1603.07785 [hep-ph].
27. F. Caporale, F.G. Celiberto, G. Chachamis, D.G. Gómez and A. Sabio Vera, arXiv:1606.00574 [hep-ph].
28. G. Chachamis, M. Deak, A. Sabio Vera and P. Stephens, Nucl. Phys. B **849** (2011) 28 [arXiv:1102.1890 [hep-ph]].
29. G. Chachamis and A. Sabio Vera, Phys. Lett. B **709** (2012) 301 [arXiv:1112.4162 [hep-th]].
30. G. Chachamis and A. Sabio Vera, Phys. Lett. B **717** (2012) 458 [arXiv:1206.3140 [hep-th]].
31. G. Chachamis, A. Sabio Vera and C. Salas, Phys. Rev. D **87** (2013) 1, 016007 [arXiv:1211.6332 [hep-ph]].
32. G. Chachamis and A. Sabio Vera, JHEP **1602** (2016) 064 doi:10.1007/JHEP02(2016)064 [arXiv:1512.03603 [hep-ph]].

Kantowski-Sachs and Bianchi models in Einstein-Dilaton-Gauss-Bonnet gravity

Luca Parisi
Dipartimento di Fisica "E.R.Caianiello", Università di Salerno,
INFN, Sezione di Napoli, GC di Salerno
Via Giovanni Paolo II, 132, 84084 Fisciano (Sa), Italy

Abstract

Some homogeneous cosmological models, namely Bianchi type I, Bianchi type III and Kantowski-Sachs, are considered in the framework of Einstein-dilaton-Gauss-Bonnet gravity. The cosmological equations are presented and the conditions for the occurrence of a bounce are briefly discussed.

1 Introduction

During the last decades many theories aiming to extend Einstein's General Relativity (GR) in order to accommodate the current observations from astrophysics and cosmology have been put forward. Here we consider the so-called Einstein-Dilaton-Gauss-Bonnet (EdGB) gravity, a theory which emerges naturally from different possible fundamental theories.

From the point of view of higher-dimensiona theories, the Gauss-Bonnet term, together with the Ricci scalar, realizes the Lovelock gravity Lagrangian in four dimensions. Even though it is topological, in EdGB gravity the Gauss-Bonnet invariant is coupled to a scalar field (namely, the dilaton field) producing a non-vanishing contribution to the equations of motion. Moreover, this term often appears as a corrections as suggested by low-energy effective string theories.

From a different point of view, among the so called extended theories of gravity, which aim to generalize the Einstein-Hilbert action considering general functions of curvature invariants, EdGB gravity is particularly interesting since its higher order curvature terms lead to second order field equations, thus avoiding the Ostrogradskys instability.

The (non-minimally coupled) Gauss-Bonnet term added to the Einstein-Hilbert lagrangian plays an important role when higher order corrections become relevant such as in cosmology [1)] and black hole physics [2)] (see also [3)] and references therein).

Recently Friedmann-Robertson-Walker bouncing cosmological models have been investigated in string-inspired Gauss-Bonnet gravity [4, 5, 6)]. It is worth to extend these investigations to less symmetric models since the behaviour of the universe at a bounce might be different when departing from the isotropic and spatially homogeneous symmetry. For this reason, here we consider Kantowski-Sachs and Bianchi models following an approach introduced in the framework of General Relativity [7)] which has already proved to be useful when dealing with modified theories of gravity [8, 9)].

2 The EdGB action

The theory under consideration is described by the following action:

$$S = \frac{1}{2}\int d^4x\,\sqrt{-g}\left[R - \frac{1}{2}\partial_\mu\Phi\partial^\mu\Phi + \frac{\alpha e^\Phi}{4}\mathcal{R}^2_{GB}\right], \tag{1}$$

where g is the determinant of the metric tensor, Φ is the dilaton i.e. a scalar field coupled to the Gauss-Bonnet invariant:

$$\mathcal{R}^2_{GB} = R^2 - 4R_{\alpha\beta}R^{\alpha\beta} + R_{\alpha\beta\gamma\delta}R^{\alpha\beta\gamma\delta} \tag{2}$$

In what follows we consider α as an unspecified coupling constant even thought it can be connected to the Regge slope parameter and to an additional parameter which, in turn, depends on the underling types of string theories (bosonic, heterotic, and superstrings, respectively). The equation of motion for the scalar field and the Einstein equation are found by varying this action with respect to the dilaton and the metric tensor respectively. They read:

$$\frac{1}{\sqrt{-g}}\partial_\mu\left(\sqrt{-g}\partial^\mu\Phi\right) = -\frac{\alpha}{4}e^\Phi\mathcal{R}^2_{GB}, \tag{3}$$

and

$$R_{\mu\nu} - \frac{1}{2}g_{\mu\nu}R = \frac{1}{2}\partial_\mu\Phi\partial\nu\Phi - \frac{1}{4}g_{\mu\nu}\partial_\rho\Phi\partial^\rho\Phi - \alpha\mathcal{K}_{\mu\nu}, \tag{4}$$

with

$$\mathcal{K}_{\mu\nu} = \left(g_{\mu\rho}g_{\nu\lambda} + g_{\mu\lambda}g_{\nu\rho}\right)\eta^{\kappa\lambda\alpha\beta}D_\gamma\left[\tilde{R}^{\rho\gamma}{}_{\alpha\beta}\partial_\kappa f\right] \tag{5}$$

and $\eta^{\mu\nu\rho\sigma} = \epsilon^{\mu\nu\rho\sigma}(-g)^{-1/2}$, $\eta^{0ijk} = -\epsilon_{ijk}$, $\tilde{R}^{\mu\nu}{}_{\alpha\beta} = \eta^{\mu\nu\rho\sigma}R_{\rho\sigma\alpha\beta}$, $f = \frac{e^\Phi}{8}$. For the seek of simplicity, here we have neglected the potential for the dilaton field.

3 Cosmological equations for homogeneous spaces

In what follows we consider the metric

$$ds^2 = -dt^2 + A(t)^2\ dr^2 + B(t)^2\left[d\theta^2 + F(\theta)^2 d\phi^2\right]$$

corresponding to Kantowski-Sachs for $F(\theta) = \sin(\theta)$, Bianchi-III for $F(\theta) = \sinh(\theta)$ and LRS Bianchi-I for $F(\theta) = 1$ respectively. With this choices for the space-time geometry, the Gauss-Bonnet scalar reads:

$$\mathcal{R}^2_{GB} = 8\left[\frac{\ddot{A}}{A}\left(\frac{\dot{B}^2}{B^2} - \frac{\zeta}{B^2}\right) + 2\frac{\dot{A}\dot{B}\ddot{B}}{AB^2}\right], \tag{6}$$

where $\zeta = \frac{F''}{F}$ and F'' represents the second derivative with respect to θ so that ζ is $-1, 1, 0$.

The Esinstein equations in Eq.(4) and the equation of motion for the dilaton field in Eq.(3) finally read:

$$
\begin{aligned}
2\frac{\dot{A}\dot{B}}{AB} - \frac{\zeta}{B^2} + \frac{\dot{B}^2}{B^2} &= \frac{1}{4}\dot{\Phi}^2 - \alpha\frac{(-\zeta + 3\dot{B}^2)\dot{A}\dot{\Phi}e^{\Phi}}{AB^2} && (7)\\
2\frac{\ddot{B}}{B} - \frac{\zeta}{B^2} + \frac{\dot{B}^2}{B^2} &= -\frac{1}{4}\dot{\Phi}^2 - \alpha\frac{\left[(-\zeta + \dot{B}^2)(\ddot{\Phi} + \dot{\Phi}^2) + 2\dot{B}\ddot{B}\dot{\Phi}\right]e^{\Phi}}{B^2} && (8)\\
\frac{\dot{A}\dot{B}}{AB} + \frac{\ddot{A}}{A} + \frac{\ddot{B}}{B} &= -\frac{1}{4}\dot{\Phi}^2 - \alpha\frac{\left[(\dot{A}\dot{B}\dot{\Phi})^{\cdot} + (\dot{A}\dot{B}\dot{\Phi}^2)\right]e^{\Phi}}{AB} && (9)\\
\ddot{\Phi} + \dot{\Phi}\left(\frac{\dot{A}}{A} + 2\frac{\dot{B}}{B}\right) &= 2\alpha e^{\Phi}\left[\frac{\ddot{A}}{A}\left(\frac{\dot{B}^2}{B^2} - \frac{\zeta}{B^2}\right) + 2\frac{\dot{A}\dot{B}\ddot{B}}{AB^2}\right]. && (10)
\end{aligned}
$$

In order to study the conditions for a bounce it is also useful to define an expansion parameter for each scale factor thus, following [8], we set

$$
H_a = \frac{\dot{A}}{A} \quad \text{and} \quad H_b = \frac{\dot{B}}{B}. \tag{11}
$$

Using these definitions, Eqs.(7)-(10) read:

$$
2H_aH_b - \frac{\zeta}{B^2} + H_b^2 = \frac{1}{4}\dot{\Phi}^2 - \alpha\left(-\frac{\zeta H_a}{B^2} + 3H_aH_b^2\right)\dot{\Phi}e^{\Phi}
$$

$$
2\dot{H}_b + 3H_b^2 - \frac{\zeta}{B^2} = -\frac{1}{4}\dot{\Phi}^2 - \alpha e^{\Phi}\left[\left(-\frac{-\zeta}{B^2} + H_b^2\right)(\ddot{\Phi} + \dot{\Phi}^2) + 2H_b(\dot{H}_b + H_b^2)\dot{\Phi}\right]
$$

$$
\dot{H}_a + H_a^2 + \dot{H}_b + H_b^2 + H_aH_b = -\frac{1}{4}\dot{\Phi}^2 -
$$

$$
\alpha e^{\Phi}\left[\left((\dot{H}_a + H_a^2)H_b + (\dot{H}_b + H_b^2)H_a\right)\dot{\Phi} + H_aH_b(\ddot{\Phi} + \dot{\Phi}^2)\right]
$$

$$
\ddot{\Phi} + \dot{\Phi}\left(H_a + 2H_b\right) = 2\alpha e^{\Phi}\left[(\dot{H}_a + H_a^2)(H_b^2 - \frac{-\zeta}{B^2}) + 2H_aH_b(\dot{H}_b + H_b^2)\right].
$$

A bounce in the scale factor A occurs at time $t = t_0$ if and only if $H_a(t^*) = 0$ and $\dot{H}_a(t^*) > 0$, the analogous conditions holding in order to have the bounce in B. Hence, in general there can be a bounce in just one of the two scale factors.

Making use of these definitions it can be immediately seen, eg. from the third equation, that the above-stated conditions can't be fulfilled simultaneously. Indeed, by imposing $H_a(t^*) = H_b(t^*) = 0$ one would get

$$
\dot{H}_a(t^*) + \dot{H}_b(t^*) = -\frac{1}{4}\dot{\Phi}^2 \tag{12}
$$

thus a simultaneous bounce in A and B at time t^* is impossible.

The conditions imposed in the previous example are quite restrictive. Indeed, a bounce can be defined in terms of volume expansion scalar θ, the shear scalar $\sigma^2 = \frac{1}{2}\sigma^{\mu\nu}\sigma_{\mu\nu}$ (where $\sigma^{\mu\nu}$ is the shear tensor) and the 3-curvature scalar ${}^{(3)}R$ of the geodesic congruence generated by the timelike unit vector field ∂_t. Moreover, under less the restrictive conditions (stated above) a bounce can occur in a single scale factor. In both cases the situation is way more complicated and deserve further investigations.

4 Conclusions

We have presented the cosmological equations for homogeneous space-times in EdGB gravity. We have defined the conditions under which a *bounce* can occur in one of the scale factors and we have considered the simplest possible example. A full-fledged analysis of the above considered models, where the role played by the the modification of the Einstein-Hilber action due to the non-minimally coupled Gauss-Bonnet term is discussed, will be subject of a forthcoming paper [10]. A qualitative analysis of the phase space along with a description of other interesting physical features (isotropisation, recollapse, etc.) will be provided.

Acknowledgments

This work is partially supported by Agenzia Spaziale Italiana (ASI) through contract n.I/034/12/0, by Istituto Nazionale di Fisica Nucleare (INFN) and by the Itailan Ministero dell'Istruzione, dell'Università e della Ricerca (MIUR).

References

1. A. De Felice and S. Tsujikawa, "f(R) Theories", Living Rev. Relativity 13, (2010), http://www.livingreviews.org/lrr-2010-3

2. P. Kanti, N. E. Mavromatos, J. Rizos, K. Tamvakis and E. Winstanley, Phys. Rev. D **54**, 5049 (1996) [hep-th/9511071].

3. A. Maselli, P. Pani, L. Gualtieri and V. Ferrari, Phys. Rev. D **92**, 083014 (2015)

4. A. Escofet and E. Elizalde, arXiv:1510.05848 [gr-qc].
5. K. Bamba, A. N. Makarenko, A. N. Myagky and S. D. Odintsov, JCAP **1504**, no. 04, 001 (2015).
6. K. Bamba, A. N. Makarenko, A. N. Myagky and S. D. Odintsov, Phys. Lett. B **732**, 349 (2014).
7. S. Byland and D. Scialom, Phys. Rev. D **57** (1998) 6065.
8. D. M. Solomons, P. Dunsby and G. Ellis, Class. Quant. Grav. **23** (2006) 6585.
9. T. Singh, R. Chaubey and A. Singh, Int. J. Mod. Phys. A **30** (2015) no.14, 1550073.
10. L. Parisi, G. Lambiase and G. Vilasi, in preparation.